ABSTRACT

Title of Thesis: GROWTH AND FMR CHARACTERIZATION OF IN-PLANE MAGNETIZATION GARNET THIN-FILMS

Degree Candidate: Jing Zhang

Degree and Year: Master of Science, 2004

Thesis directed by: Professor Isaak D. Mayergoyz
Department of Electrical Engineering and Computer Engineering

Planar magnetization Bi-doped garnet thin-films were successfully grown for magneto-optical imaging applications. These films are grown using the liquid phase epitaxy method, which produces single crystal, high quality films.

The melt composition that is used to grow these garnets is selected in order to produce planar magnetization films with low magneto-crystalline and uniaxial anisotropies. Also, this melt composition is designed to incorporate more bismuth into the film, thereby increasing the specific Faraday rotation of the film. This effectively tailors the films to be highly sensitive to spatial magnetic field distributions.

The garnet films that are grown from this process are characterized by measuring their ferromagnetic resonance, which allows their magneto-crystalline and uniaxial anisotropies to be determined.

An imager system that utilizes these garnet films has also been developed to visualize magnetic recording from cassette tapes. The Federal Bureau of Investigation (FBI) uses these captured images for forensic applications.

GROWTH AND FMR CHARACTERIZATION OF IN-PLANE MAGNETIZATION GARNET THIN-FILMS

by

Jing Zhang

Thesis submitted to the Faculty of the Graduate School of the
University of Maryland, College Park in partial fulfillment
of the requirement for the degree of
Master of Science
2004

Advisory committee:

Professor Isaak D. Mayergoyz, Chair/Advisor
Professor Julius Goldhar
Associate Professor Romel Gomez

ACKNOWLEDGEMENT

I would like to thank Professor Isaak Mayergoyz for his guidance and advice throughout this project. I would like thank Dr. Charles Krafft for conceiving the idea of this research. I would also like to thank Dr. Krafft for his support and supervision while working on this project. I would like to thank Iulian Nistor for his support in growing the garnet films. Finally, I would like to thank Rafael Rojas for the mismatch data he collected.

TABLE OF CONTENTS

LIST OF FIGURES

Chapter 1 - Introduction

It is well known that magneto-optical materials that utilize the Faraday rotation are useful for visualizing and imaging magnetic domains and spatial magnetic field distributions. The properties of these magneto-optical materials have been investigated since the late 1960's [1]

Most magneto-optical materials yield low-resolution magnetic structures due to their low specific Faraday rotation [2]. For applications that require finer resolution, ferrimagnetic films that include bismuth are more suitable, since this inclusion dramatically increases the specific Faraday rotation [2]. Thus, Bi-doped iron garnet films have been developed. These garnet films have a broad operation frequency range in both the visible and infrared spectrum thus making them ideal for many applications. Also, these films can be grown using the liquid phase epitaxy method. This method produces low defect single crystal structure films.

The Bi-doped iron garnet films are used in many applications. One such application is the detection of current inside superconducting samples. For this, the garnet films are used to visualize the stray magnetic fields of the superconductors [2]. Vortices inside the superconductors can also be imaged by using these garnet thin-films. Recently, non-destructive evaluations of micro-cracks and surface defects in conducting materials for industrial applications have been done using both in-plane and perpendicular magnetization Bi-doped iron garnet thin-films [3].

For this study, Bi-doped lutetium iron garnet (BIG) thin-films are developed for forensic imaging of magnetic media. These films are grown on (100) gadolinium gallium garnet (GGG) substrates using the liquid phase epitaxy method. These films are designed

to have high sensitivity and low magneto-crystalline anisotropy. For greater spatial resolution, the films are grown to have planar magnetization [9]. Also, a wideband microwave apparatus is built to perform ferromagnetic resonance (FMR) characterization of the grown films. An imager system using the garnet thin-films is developed for the purpose of forensic imaging applications. This imager system has since been delivered to the Federal Bureau of Investigation.

Garnets and their special properties:

Magnetic garnets have properties that make them ideal for many electronic and magneto-optical devices. Garnets are ionic crystals that are comprised of a body center cubic crystal structure such that each unit cell containing eight formula units of $\{C\}_3[A]_2(D)_3X_{12}$, where C is a large dodecahedral site, A is a moderately sized octahedral site, D is a small tetrahedral site, and X is an anion site that is most commonly occupied by oxygen [5]. The unit cell of garnet contains 160 ions. The unit cell of the garnet is depicted in Figure 1 [6]. Although there are many different types of naturally formed garnets, synthetic garnets are of special interest. This is due to their enhanced magneto-optical properties.

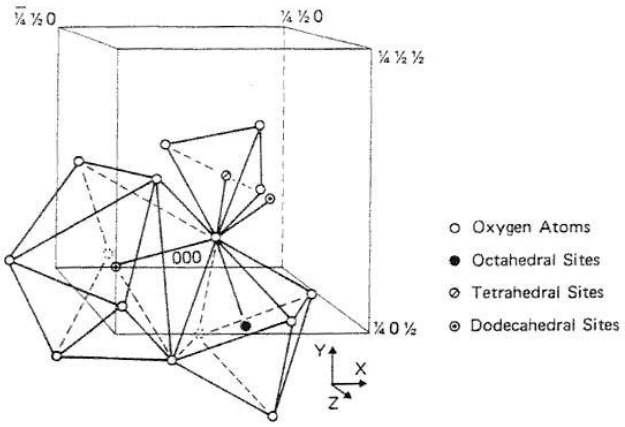

Figure 1 - Crystal Structure of one unit cell of magnetic garnet [6]

One example of a synthetic garnet with enhanced optical properties is the rare-earth iron garnet $\{RE\}_3[Fe]_2(Fe)_3O_{12}$ (RIG) [5]. This ferromagnetic garnet consists of octahedral and tetrahedral sites that are antiferromagnetically coupled to each other. The difference in the number of sites provides a net magnetic moment equivalent to one Fe^{3+} ion [5]. If the RE element is nonmagnetic, then the iron ions form two non-ideal anti-parallel sublattices. This is what classifies the garnet as ferrimagnetic [7].

The superexchange interactions between pairs of sublattices are strongest when the sublattices are parallel to each other. Conversely, these interactions are weakest when the sublattices are perpendicular to each other [7]. Since the Fe^{3+} ions only occupy the octahedral sites, the sublattices occupied by these ions strongly interact with each other at an angle of 126.6º. However, the sublattice occupied by the RE and the sublattice occupied by the Fe^{3+} ion have a weaker coupling between them at an angle of only 100º [7]. The net magnetization of the garnet is defined as

$$M_s(T) = \left| \pm \vec{M}_c(T) - \vec{M}_a(T) + \vec{M}_d(T) \right|$$

where $M_c(T)$, $M_a(T)$, and $M_d(T)$ are the temperature dependent magnetizations of the dodecahedral, octahedral, and tetrahedral sublattices, respectively [5]. Given this equation, it can be seen that if diamagnetic ions, such as gallium or aluminum, are substituted at the tetrahedral site for iron, the saturation magnetization of the garnet is reduced.

Two common types of RIG are the yttrium iron garnet $\{Y^{3+}\}_3[Fe]_2(Fe)_3O_{12}$ (YIG) and bismuth iron garnet $\{Bi^{3+}\}_3[Fe]_2(Fe)_3O_{12}$ (BIG) [2]. The Y^{3+} and the Bi^{3+} ions on the dodecahedral lattice have weak magnetic moments by themselves; however they will align parallel with the octahedral lattice and anti -parallel with the tetrahedral lattice, which enhances the overall magnetic moment [2].

The magnetic moment of the Y^{3+} and Bi^{3+} ions increases as the temperature decreases. The Y^{3+} and Bi^{3+} ions differ in that Bi^{3+} has a larger ionic radius of 1.17 Å than the Y^{3+} with ionic radius of .95 Å [7]. This difference in ion size results in a larger lattice parameter for BIG and thus slightly reduces the saturation magnetization value [7].

The yttrium iron garnet $Y_3Fe_5O_{12}$ (YIG) has low microwave absorption, making it ideal for applications involving microwave filtering and oscillation. Also, when substituted with elements such as europium, calcium, and germanium, these yttrium garnet films can also be used for bubble memory applications [3]. However, the YIG crystal can only provide a small amount of Faraday rotation (about .08 deg/μm) which is not sufficient for the development of integrated magneto-optical devices [3]. The incorporation of bismuth in the iron-garnet greatly increases the Faraday rotation (about -8 deg/μm at 633 nm wavelength), thus making it an ideal material for magneto-optical

indicators [22]. The increase in Faraday rotation is proportional to the amount of bismuth that is incorporated into the garnet film [7].

Faraday Effect

The Faraday Effect describes the phenomenon in which an external magnetic field causes the rotation of the polarization plane of a linearly polarized light beam that passes through a material. The equation used to describe the Faraday relationship is of the form

$$\theta(\omega) = V(\omega)\vec{B} \cdot \vec{L} \qquad (1)$$

where, $\theta(\omega)$ is the degree of rotation, $V(\omega)$, is the Verdet constant that is inherent to the properties of the material, $\vec{B}$ is the magnetic induction, and $\vec{L}$ optical path length. This relationship states that the degree of rotation is directly proportional to both the magnetic induction and optical path length. Since the magnetic induction, $\vec{B} = \mu_0(\vec{H}_0 + \vec{M}_s)$, includes the magnetization of the material and the external field (where $M_s = \mu_r H$), then from (1) it can be seen that the Faraday rotation is proportional to the component of the magnetization vector that is co-linear to the direction of light propagation.

It can also be seen from (1) that the Faraday effect is nonreciprocal phenomenon. Thus, if a beam of light is transmitted through the material, reflected, and transmitted back through it, the rotation of the polarization plane of the beam doubles. A graphical representation demonstrating the nature of this nonreciprocal effect is shown in Figure 2.

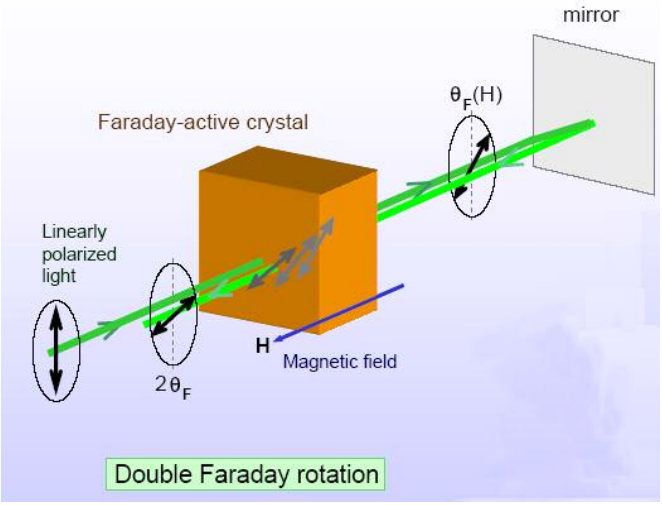

Figure 2 - Graphical representation of the double Faraday effect [8]

There are two theories that can be used to explain the Faraday effect, the classical theory and the quantum-mechanical theory. The classical theory, also known as Becquerel's theory, states that linearly polarized light can be represented as the combination of a left circularly polarized (LCP) beam and a right circularly polarized (RCP) beam that encounter different optical paths lengths in the material. The difference in the optical path lengths is due to a polarization dependence of the index of refraction of the material. This difference results in a phase difference between the two polarization states. This phase difference is equivalent to a rotation in the polarization plane of the incident linearly polarized light. Becquerel's theory models an electron rotating about the nucleus of the atom with a spring-like interaction between the two. The diagram depicting this model is shown in Figure 3. The steady state solution for this model is

$$-m\omega^2 r = -kr + qE \pm \frac{qB\omega r}{c} \tag{2}$$

The ± corresponds to LCP or RCP light. Also, k is analogous to the spring constant, and q and m are the electron charge and the mass, respectively.

Solving for r gives

$$r = \frac{\frac{qE}{m}}{\omega_0^2 - \omega^2 \pm \frac{qB\omega}{mc}} \tag{3}$$

where $\omega_0^2 = k/m$ is the resonant frequency of the system. Also, it should be noted that the quantity qB/m is known as the Larmor frequency, which is equal to the rotation frequency of the electron rotating about the magnetic field lines.

The electric polarization of a material can be described as

$$P = Nqr \tag{4}$$

where N is the density of the active ions. This polarization can be related to the relative permittivity of the material by

$$\varepsilon_r = \left(1 + \frac{4\pi P}{E}\right) \tag{5}$$

Substituting r and P into (5), gives

$$\varepsilon_r = \left(1 + \frac{\frac{4\pi N q^2}{m}}{\omega_0^2 - \omega^2 \pm \frac{qB\omega}{m}}\right) \tag{6}$$

Since $n = \sqrt{\varepsilon_r}$, the index of refraction for RCP is

$$n_r(\omega) = \sqrt{1 + \frac{\frac{4\pi N q^2}{m}}{\omega_0^2 - \omega^2 - \frac{qB\omega}{m}}} \tag{7}$$

and the index of refraction for LCP is

$$n_l(\omega) = \sqrt{1 + \frac{\frac{4\pi N q^2}{m}}{\omega_0^2 - \omega^2 + \frac{qB\omega}{m}}} \tag{8}$$

The phase difference due to different LCP and RCP optical path lengths is

$$\theta = \frac{\pi(n_l - n_r)L}{\lambda} \tag{9}$$

where L is the length of the material that the light passes through, and is the optical wavelength. For small differences in the refractive indices for LCP light and RCP light, (9) can be expanded as a Taylor series

$$(n_l - n_r) = \frac{dn}{d\omega}(\Delta\omega_l - \Delta\omega_r) = \left(\frac{dn}{d\lambda}\right)\left(\frac{\lambda^2}{2c\pi}\right)\left(\frac{Bq}{mc}\right) \tag{10}$$

Substituting equation (10) into the equation (9) gives,

$$\theta = -\frac{dn}{d\lambda}\frac{\lambda}{2c^2}c\frac{q}{m}\cdot L \cdot B \tag{11}$$

where

$$V(\omega) = -\frac{dn}{d\lambda}\frac{\lambda}{2c^2}c\frac{q}{m} \tag{12}$$

is known as the Verdet constant. These equations show, as was previously stated, that the two circularly polarized light beams will travel different optical path lengths resulting in a phase difference of θ. This phase difference results in the rotation of the polarization plane of the linearly polarized light.

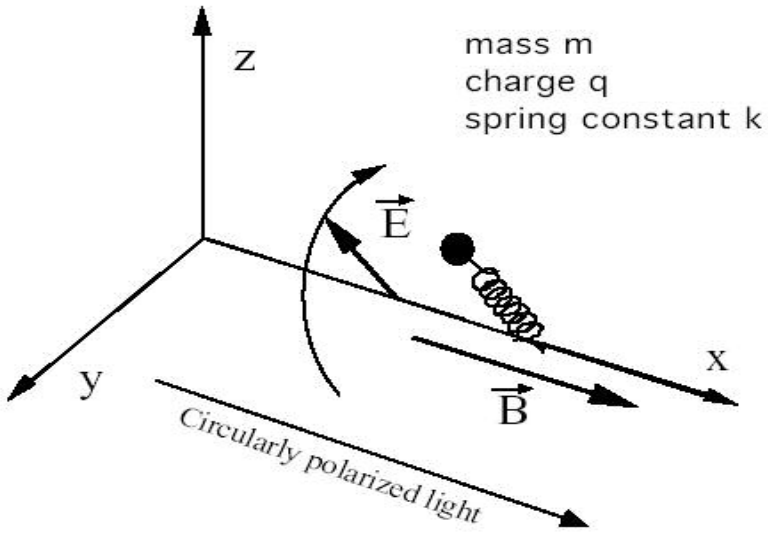

Figure 3 - Spring model representing the Becquerel's model for the Faraday effect

The quantum explanation of Faraday rotation effect starts with considering the Zeeman splitting of the atomic energy levels in the presence of a magnetic field (due to spin orbit interactions). Since the LCP and the RCP light are subject to different selection rules, different electrical dipole transitions are induced. Figure 4 shows the different transition of the LCP and RCP light.

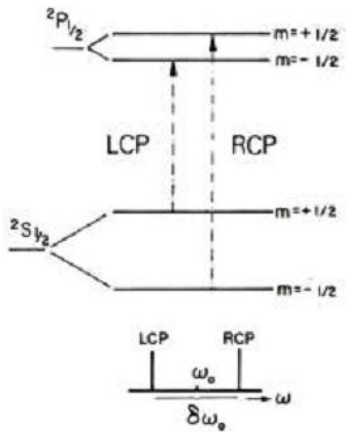

Figure 4 - Transition of LCP and RCP light and the resulting phase difference of the polarized light.

The quantum-mechanical model of the Faraday rotation can be described by

$$\theta_F = \frac{\pi e^2 \omega^2}{nmc} \sum_{i=a,d} \frac{Nf_i}{\omega_i} \left\{ \frac{(\omega_i + \Delta_i)^2 - \omega^2 - \Gamma_i^2}{[(\omega_i + \Delta_i)^2 - \omega^2 - \Gamma_i^2] + 4\omega^2\Gamma_i^2} - \frac{(\omega_i - \Delta_i)^2 - \omega^2 + \Gamma_i^2}{[(\omega_i - \Delta_i)^2 - \omega^2 + \Gamma_i^2] + 4\omega^2\Gamma_i^2} \right\} \quad (13)$$

where ω_i is resonance energy, Δ_i is the spin orbit splitting energy, f_i is the oscillator strength, and Γ_i is the half linewidth of the transition [9].

Due to covalent interaction, the Bi^{3+} causes the splitting of the Fe^{3+} degenerate orbital, thus enhancing the Faraday rotation. Specifically, the overlap between the 6p orbit of Bi^{3+}, 2p orbit of O^{2-} and 3d orbit of Fe^{3+} results in a spin orbit splitting of $2\Delta i$. The additional atomic transitions due to the inclusion of bismuth enhance the Faraday rotation because each transition is subject to the same selection rule for the electric dipole

transitions, as shown in Figure 5. In this figure, the (+1) and (-1) represents the selection rule for the RCP and LCP light respectively.

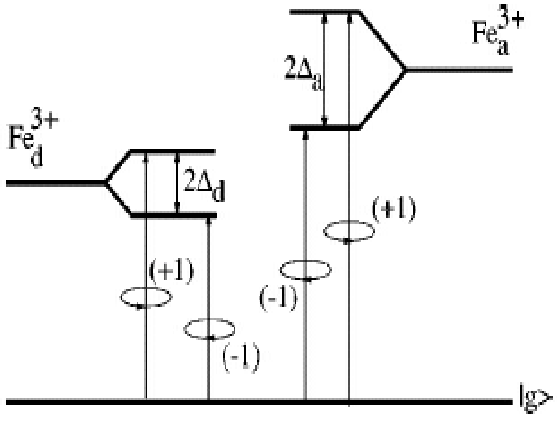

Figure 5 - Additional transitions due to the inclusion of bismuth

Many applications have been developed to utilize the properties of bismuth substituted iron garnet films. The high Faraday rotation of these garnet films causes a significant rotation of the light's polarization plane. The degree of rotation of the light's polarization plane is directly proportional to the strength of the magnetic induction. This property allows garnet thin-film to be used as the sensing element in high frequency, low noise magneto-optical sensors. Also, the non-reciprocal property of the Faraday rotation effect makes the garnet films ideal for optical isolators. Additionally, these magneto-optical films can be used as indicators that are used for the real-time imaging of magnetic patterns [3].

Magnetic Anisotropy in Ferrimagnetic Garnet Films:

The magnetic anisotropy in ferrimagnetic garnet films originates from four different sources [5]. The first of these sources is the ordering of dodecahedral ions along the growth direction. This causes growth-induced uniaxial anisotropy. Growth-induced anisotropy can be classified as either one of two types: the anisotropy between rare-earth pairs and the anisotropy between bismuth and a rare-earth [23]. The anisotropy between bismuth and a rare-earth depends on the way that the bismuth is incorporated, and on the way that the rare-earth ion is interacting with the bismuth [23]. It has been shown that the heavy rare-earth elements tend to have the lowest growth-induced anisotropies in the <111> growth direction when coupled with Bi. Other studies have shown that Bi-Lu based iron garnets have near zero anisotropy [10]. Growth-induced anisotropy can be reduced through the substitution of diamagnetic ions on both the tetrahedral and octahedral sites [5].

The second source of magnetic anisotropy is magneto-crystalline anisotropy. This anisotropy is an intrinsic property of the garnet crystal. Due to this anisotropy, the magnetization of the garnet possesses energy minima along directions known as “easy” axes. Rotating between two easy axes requires crossing an energy barrier [19]. The magnitude of this barrier is described by a constant called the magneto-crystalline anisotropy The chemical composition of the garnet determines the orientation of the easy axes and their degree of anisotropy [13]. The magneto-anisotropy constants K_1 and K_2 (with the subscript defining the order) are typically very small, with K_2 much less than K_1, thus K_2 can usually be ignored [13]. A negative K_1 value results in easy axes that are oriented along the <111> crystalline directions, while a positive K_1 value results in easy

axes that are along the <100> crystalline directions [13]. The K_1 value varies with temperature, and the dilution with gallium makes this temperature variation larger. The magneto-crystalline anisotropy can be reduced by the careful selection of rare-earth elements and by the dilution of octahedral iron through diamagnetic substitution [13].

The third source of magnetic anisotropy is stressed-induced anisotropy. This arises from the compressive and tensile strain applied on the rare-earth iron garnet through the mismatched lattice between the film and the substrate. This mismatch induces a uniaxial anisotropy [13]. The garnets have negative magnetostrictive coefficients in both the <111> and <100> directions giving them negative uniaxial anisotropy for tension and positive uniaxial anisotropy for compression [13]. At a given constant temperature, it is possible to eliminate the effects of stressed-induced anisotropy with growth-induced anisotropy [13].

The last source of magnetic anisotropy is the demagnetization effects, also known as shape anisotropy. These effects are due to virtual magnetic charges which are present whenever there is a discontinuity of the magnetization. Shape anisotropy is determined by the demagnetizing energy of the garnets to favor planar magnetization in the (100) films. This demagnetizing energy is proportional to the square of the saturation magnetization ($4\pi M_s^2$) [19]. Similarly, the negative uniaxial demagnetization field is linearly proportional to the $4\pi M_s$ value, thus the shape anisotropy is reduced as the saturation magnetization is reduced.

Requirements for Growing Ideal MOI

In order to be an ideal magneto-optical indicator (MOI), the Bi-doped garnet films have to meet certain criteria. Specifically, the garnet films must have high sensitivity, high spatial resolution, and a large range of detectable field strengths in order for the garnets to be useful in obtaining magnetic information.

The sensitivity of the MOI film is dependent on the specific Faraday rotation of the film, the thickness of the film, and the response of the MOI magnetization to the sample field. It is also related to the distance of the sample from the MOI film [5]. The sensitivity of the MOI film can be expressed as

$$\frac{d\theta}{dH} = \theta_s t \frac{d\sin(\alpha)}{dH} \tag{14}$$

where θ is the local Faraday rotation, H is the local magnetic field experienced by the MOI film, θ_s is the specific Faraday rotation per unit thickness, t is the film thickness, and α is the angle of the magnetization vector to the film normal [9].

The specific Faraday rotation is determined by the amount of bismuth concentration in the film. The inclusion of bismuth results in dislocations in the material that limit the maximum amount of bismuth that can be incorporated into the film. The onset of these dislocations occurs when the amount of bismuth that is incorporated into the material reaches a value of 1.0-1.3 atoms per formula unit [25]. These dislocations are also dependent on the substitution level of diamagnetic ions such as Ga, as well as on the growth temperature [25].

At incident optical signal with lower wavelengths, the dispersion relation of the garnet produces a higher Faraday rotation [9]. This rotation is limited by the absorption edge of the material, which is typically around 500 nm. Additionally, the Fe^{3+} induces an absorption band near the 900 nm [9]. Due to these two limitations, the Bi-doped garnet film ideally operates in the visible range. However, the operating temperature of the MOI film should also be considered, since as this temperature increases, the specific rotation decreases [9].

The total saturated Faraday rotation, θ, is equal to the product of θ_s and t (the thickness of the film). Thus, thicker films produce higher angle of rotation. The thickness of the film also affects the resolution and the sensitivity, since these thicker films absorb more light and thus decrease the signal strength [5].

The feature size of the film is directly proportional to the thickness of the film [9]. Thus, a smaller feature size is possible through the reduction of film thickness [9]. For materials that exhibit a higher level of sensitivity, thinner films may be used to increase the resolution of the image.

The separation between the sample and the MOI film is important because the strength of magnetic field is inversely proportional to the third power of this separation. The overall separation between the film and the sample is limited by the flatness of their contact surface. Since both materials are rigid, a non-uniform surface will result in gaps between the two materials. Thus, the surface of the substrate and the MOI film must be uniform in order to have good signal strength and resolution. These requirements set the criteria for the growth conditions of the Bi-doped garnet films.

The response of the film is dependent on the effective anisotropy field, H_k^{eff} . The effective anisotropy is the combination of the uniaxial magnetic anisotropy and the saturation magnetization fields and is defined by

$$H_k^{eff} = \frac{8\pi K_u}{4\pi M_s} - 4\pi M_s \qquad (15)$$

where K_u is the overall uniaxial anisotropy. When, H_k^{eff} is negative, $\sin(\alpha)$ from equation (14)will be equal to H/H_k^{eff} [9]. This negative effective anisotropy can be influenced non-uniformly by the cubic magnetocrystalline anisotropy [9].

The range of detectable field strengths of the bismuth garnet film is also limited by the saturation magnetization. At room temperature, the $4\pi M_s$ is about 2000 G, which corresponds to a maximum detectable field strength of 2000 Oe [5]. The saturation magnetization increases with decreasing temperature, thus increasing the range. At the same time, the sensitivity is compromised with increasing saturation magnetization [5]. For applications where no external field is applied, the importance of sensitivity surpasses that of the detectable field strengths. Therefore, for such applications, films with low $4\pi M_s$ are desirable

In order to achieve the criteria for MOI film, the garnet films must have low saturation magnetization, near zero uniaxial anisotropy, K_u, and zero cubic anisotropy. Low saturation magnetization increases the sensitivity of the film because the demagnetization field is lower. Thus, a lower magnetic field is needed to tilt the magnetization out of the film plane. Near zero uniaxial anisotropy, K_u, in combination with a low $4\pi M_s$ produces a small negative effective anisotropy field H_k^{eff}, and planar

domains [5]. Some canting of the magnetization vectors of the film is desired in order to enhance the sensitivity of the film. Canting may result in a reduction of the demagnetization field. Magnetization canting can be induced by a higher cubic magneto-crystalline anisotropy [5].

There has been extensive research investigating the growth of garnet films by varying the growth conditions and melt composition. One successful example of this is the work by Grechishkin et al [10]. Grechishkin has grown films with a $Bi_1Lu_2Fe_4Ga_1O_{12}$ composition [10]. These films were highly sensitive, making them suitable for magneto-optical imaging [10]. The effectiveness of these films is due to the use of Lu and their growth on (100) oriented substrates. These conditions cancel the growth-induced anisotropy, and at the same time, gallium dilution effectively eliminates the magneto-crystalline anisotropy [5]. At room temperature, the low saturation magnetization in these films decreases the shape anisotropy to values that are low enough to be easily overcome by weak sample fields [5]. Additional improvements to the properties of these films at room temperature may be obtained by increasing the dilution with gallium. However, care must be exerted, since dilution also reduces the Faraday effect. Thus there is an upper limit to the acceptable amount Ga dilution.

Chapter 2 - Growth of Garnet Films:

Methods of Film Growth:

A variety of methods are used to grow iron garnet films. Some common methods include liquid phase epitaxy (LPE), implantation, reactive ion beam sputtering, and pulsed laser deposition. The disadvantage in implantation and pulsed laser deposition is that these methods do not produce defect free single crystal structures, whereas the disadvantage of the sputtering method is that it has a very slow growth rate.

LPE Method

The method chosen to grow the Bi-doped iron garnet thin-films for this study is the LPE method. The LPE method is preferred because it produces single crystal films with few crystalline defects. However, for this method, the growing conditions are difficult to control. Also, this process does not yield films with a high degree of Bi incorporation.

In equilibrium growth conditions, bismuth can not be incorporated into the film due to its large ion size. The LPE method is based on inducing a non-equilibrium state in order to grow the Bi-iron garnet films. The chemicals within the melt do not distribute homogeneously, thus a high temperature solution (HTS) in conjunction with the LPE method has been developed to grow the Bi iron garnet films [5]. A diagram of a typical LPE furnace geometry is shown in Figure 6. The garnet chemical mixture is held in a platinum crucible in order to minimize any chemical reactions between the crucible and the melt. The nucleation of the garnet crystals begins at the saturation temperature of the

melt. However, to increase the growth rate and the level of bismuth incorporation, the garnet films are grown at higher undercooling temperatures.

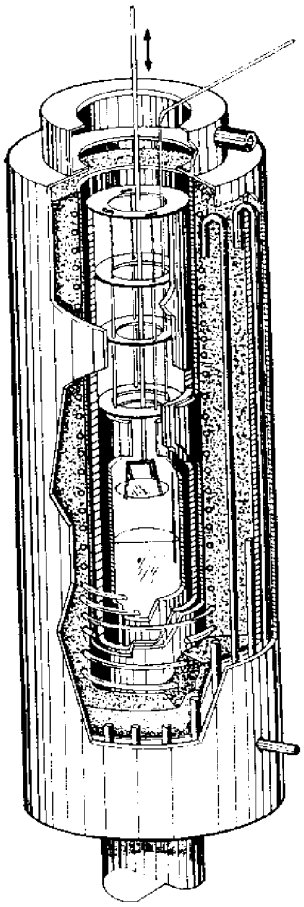

Figure 6 - Diagram of the furnace used in LPE method shown from top to bottom. [5]

In order to utilize the LPE method, the melt stability is an important parameter that must be considered. This is because undercooling of the melts aids in the incorporation of bismuth into the garnet film [3]. However, if the melt is unstable, at long periods of undercooling, spontaneous homogenous or heterogeneous nucleation can take place at the surface of the melt [5]. Thus, the degree of undercooling must be limited. The goal of the melt chemistry design and growth conditions is to maximize

undercooling. One way to prevent nucleation is to dilute the melt with more solvent. However, this prevents the growth of uniform films because the solute molecules are dispersed throughout the melt [5].

Addition of boron oxide concentration in the flux greatly enhances the melt stability [5]. The B_2O_3 molecule moves the phase boundaries on the ternary diagram closer to the RE_2O_3 [5]. The saturation temperature of the melt and the growth rates are reduced through the boron oxide addition. The nucleation rate is decreased at the surface of the melt [5]. This is because the boron oxide addition results in reduction of rare-earth oxide activity in the melt [5]. The boron oxide complexes with the rare-earth oxide to form inert clusters that do not participate in crystal growth. The complexed rare-earth oxides form a reservoir because of the kinetic balance between the active and inactive rare-earth molecules. This reservoir also prevents melt depletion effects [5].

GGG Substrate

Gadolinium gallium garnet (GGG-$Gd_3Ga_5O_{12}$, lattice parameter=12.383 Å) is commonly used as the substrate for the epitaxial growth of bismuth iron garnet [5]. GGG substrate has a close lattice match to YIG and BIG, however, due to the small lattice parameter, the incorporation of bismuth is limited. The Czochralski method can be used to grow the single crystal GGG boule. After this boule is grown, it is sliced into substrate wafers.

The growth of a garnet film on a single crystal garnet substrate prevents large mismatch between the film and the substrate and enhances the growth of the film. The

resulting film quality is strongly dependent on the quality of the substrate. If there is a lattice mismatch between the film and the substrate, cracks (film in tension) or misfit dislocations (film in compression) can form [5]. Nucleation can not occur in the case of a mismatch that is too large (approximately >2%) [5]. Since a planar magnetization in the film is desired, (100) GGG substrates are used as the basis for the film growth in order to grow planar magnetization films. It is also possible to grow films with (111) GGG substrates. However, it is more difficult to obtain planar magnetization films with these substrates.

Film Growth Process:

The films for this study are grown from a supersaturated melt that is held within a platinum crucible. The chemicals for this melt are carefully measured, mixed, and placed inside the platinum crucible. The crucible rests on top of a ceramic pedestal within the furnace chamber. The melt is homogenized for several hours at a temperature of 900 °C. A schematic of this growth apparatus is depicted in Figure 7 and a picture of the actual apparatus is depicted in Figure 8.

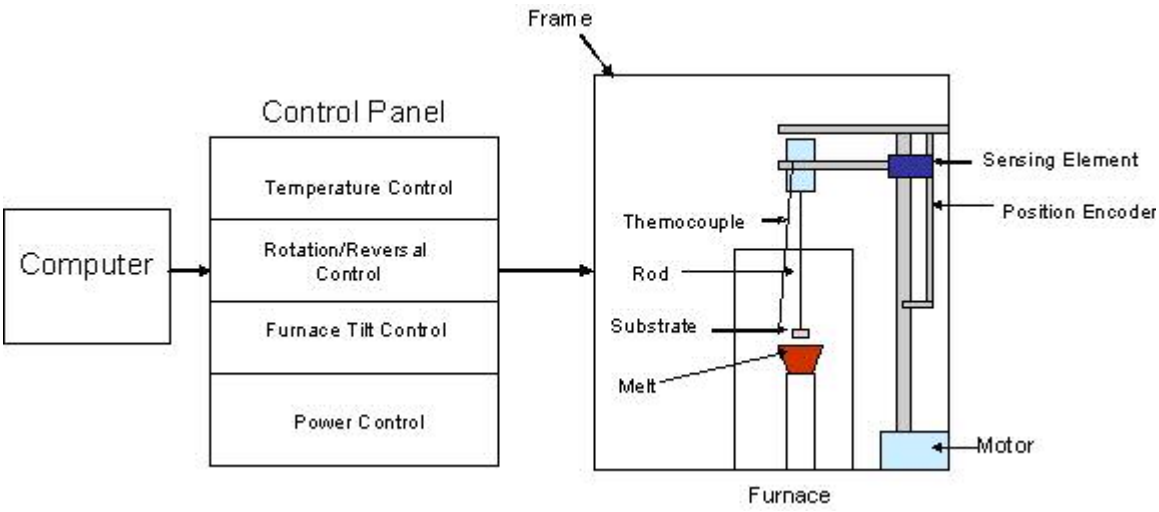

Figure 7 - Schematic of the growth apparatus

Figure 8 - Photo of the growth apparatus

The GGG substrates used for the film growth are either 1 cm^2 chips or 1 inch diameter wafers. The 1 cm^2 chips are used for a quick characterization of the melt, such as determining the saturation temperature. After initially characterizing the melt the 1 inch wafers are used to grow the film, because they have a larger surface area. The substrate is cleaned with heated diluted phosphoric acid, whereas organic material is removed from the substrate using acetone. Specially designed platinum holders are used to suspend the samples. An automated control system lowers this holder into the melt. In order for nucleation to occur, the temperature of the melt is set to a predetermined point below the saturation temperature and the melt is allowed to establish isothermal conditions. This temperature is measured with a thermo-couple that is immersed within the melt. The substrate is preheated in order to prevent it from cracking due to the high temperature variation. In order to grow film only on one side of the substrate, the substrate is lowered enough for it to barely touch the surface of the melt. The substrate is then raised ~2mm so that the surface tension will cause the melt to adhere to only one side of the film. A linear encoder determines the position of the substrate with respect to the melt.

In addition to undercooling the melt, the non-equilibrium growth conditions required for a large incorporation of bismuth can be enhanced by rotating the substrate at speeds ranging from 20 rpm to 100 rpm. However, even though more bismuth can be incorporated into the film at higher rotation speeds, the maximum rotation speed is limited because excessive rotational velocity can cause undesired surface nucleation.

After the deposition process, the substrate is removed from the melt. Spinning the substrate just above the melt surface and/or tilting the furnace are techniques for

removing the left over flux. After removing the holder from the rod, any flux that remains on the film is removed using heated nitric acid. At the end of the deposition process, the melt needs to be re-homogenized for a short time before the growth of the next film. A LABVIEW program controls the process for the film growth. The front panel diagram for this program is shown in Appendix A. A list of the parts used for the film growth process is listed in Appendix B.

Film Composition

The design of the film composition aims to achieve both high sensitivity and high spatial resolution of magnetic field distributions. These film compositions are selected in order to minimize the misfits between the film and substrate at room-temperature, thus lowering the amount of stressed-induced anisotropies. Lead oxide and boron oxide are added to the melt to act as a solvent and stabilizing element respectively within the platinum crucible. The films are grown from the melt with specific cation ratios. These ratio are listed in Table 1. The formulas used for each parameter are

$$\frac{\text{Garnet}}{\text{Flux}} = \frac{G}{F} = \frac{[Fe]+[Lu]+[Ga]}{[Pb]+[Bi]+[B]} \tag{16}$$

$$C_{Bi} = \frac{[Bi]}{[Bi]+[Pb]} \tag{17}$$

$$C_{B} = \frac{[B]}{[Bi]+[Pb]} \tag{18}$$

$$R_1 = \frac{[Fe]+[Ga]}{[RE]} \tag{19}$$

$$\frac{Fe}{Ga} = \frac{[Fe]}{[Ga]} \tag{20}$$

The growth temperatures ranged between 760° and 779° K. The melt chemistry selection controls the film composition, which has been confirmed by the electron microprobe analysis.

Melt	G/F		C^Bi		C^B	R^1	Fe/Ga
UMD40	0.234514		0.520015		0.163461	23.9907	4.999932
UMD31	0.2200		0.445		0.110	24.8	6.500

Table 1 - Cation ratios of the selected melt design

Selection of the rare-earth used in the melt is based on the anisotropy between the rare-earth and the bismuth. Studies have shown that the amount of growth anisotropy that exists between the rare-earth element and bismuth is dependent on the particular rare-earth element that is used [24]. Table 2 shows the uniaxial anisotropy constant K_g and the magneto-crystalline anisotropy constant K_1 of various rare-earth elements coupled with bismuth at room temperature. Since these numbers are highly dependent on the growth conditions, and on the concentration of bismuth and rare-earth elements in the film, the numbers in Table 2 are only used for comparison. In addition, the films in the study that provided the data for Table 2 are grown in the <111> direction, whereas the films for this study are grown in the <100> direction. As a result, the particular values for this experiment are expected to differ slightly from those in Table 2.

Rare-earth	K_g (± 10%) (10^3 erg/cm^3)	K_1 (± 25%) (10^3 erg/cm^3)
Pr	-140	
Nd	~0	-15
Sm	330	-13
Eu	200	-31
Gd	65	-7.8
Tb	156	-8.2 [48]
Dy	59	< -5 [48]
Y	69	-6
Ho	26	< -5 [48]
Er	12	-6.9
Tm	9	-7
Yb	21	-3.4
Lu	17	-5.2

Table 2- K_g and K_1 values for rare-earth elements when coupled with bismuth in (111) films at room temperature [24].

The K_1 and K_g values in Table 2 indicate that heavy rare-earth elements such as Er, Tm, Yb, Lu and Nd have the lowest magnitude growth-induced anisotropies in (111) films when coupled with Bi. Studies have also been shown that lutetium and bismuth have almost no growth-induced anisotropy in (100) films. As a result, lutetium has been selected for use in this study. Lutetium has ionic radius of 1.12 Å, which is very small compared to the ionic radius of bismuth 1.31 Å. This results in a lattice mismatch between the film and the substrate, which increases with increasing growth temperature.

The mismatch between the film and the substrate is determined by using x-ray rocking curves. The misfit of the films grown for this project is shown in Table 4. The (100) GGG substrates that are used in the film growth have lattice constants of approximately 12.38 Å. Theoretical misfit is calculated using the distances of the cation-anion distances in the formula [11].

$$a_D^2 = \mathbf{16.384}\left(m + \sqrt{m^2 - \mathbf{0.12207}\,p}\right) \tag{21}$$

where

$$m = 0.3125g^2 + 0.21875l^2 + 0.234375(t^2 + c^2) \tag{22}$$

and

$$p = 4(t^2 + c^2)^2 + 0.25(4g^2 - 2l^2 - t^2)^2 + (c^2 - 2l^2 + t^2)^2 \tag{23}$$

For these equations, *t*, *l*, *c*, and *g* are the cation-anion distances used in the film. These distances are listed in Table 3.

	C	g	l	t
CN =	8.1	8.2	6	4
Bi	5.998	6.533		
Y	5.485	5.924		
Lu	5.318	5.698	5.198	
Fe			4.064	3.516
Ga			3.996	3.415
Yb	5.322	5.794	5.189	

Table 3 - The cation-anion distances used in the lattice misfit calculations [11]

The theoretical misfits were calculated using the microprobe data on the film composition for films grown from melt UMD31 and are shown in Table 4. The cation

ratios for this melt are shown in Table 1. The actual misfits are smaller in comparison to the calculated misfits.

Film	UMD31-74	UMD31-75	UMD31-76	UMD31-77	UMD31-78	UMD31-79
Calculated Lattice (Å)	12.300	12.338	12.328	12.315	12.313	12.305
Substrate lattice (Å)	12.383	12.383	12.383	12.383	12.383	12.383
Calculated mismatch (Å)	-0.083	-0.045	-0.055	-0.068	-0.070	-0.078
Measured mismatch (Å)	-0.000133	-0.000666	-0.001066	-0.002132	-0.003197	-0.004796
Difference between measured and calculated mismatch (Å)	-0.0832	-0.04455	-0.05377	-0.06581	-0.06725	-0.07368

Table 4 - Calculated and experimental misfit data of films grown from melt UMD31.

Rotation Reversal

The growth rate of a film can be increased by periodically reversing the direction of rotation of the substrate during the growth process [12]. The incorporation of bismuth into the film is increased, since this incorporation is proportional to the growth rate of the film. It has also been shown that the amount of bismuth incorporated into the film increases as the period between reversals decreases [12]. However, this period cannot be too small because fast switching can cause increased surface motion of the melt. This disturbance can lead to a non-equilibrium state at the surface, which can generate spontaneous surface nucleation.

The effect of periodic rotation reversal has been studied on the UMD40 melt. For this, a reversal circuit has been built to control this periodic switching. The schematic for this reversal circuit is depicted in Figure 9. This circuit consists of a 555 timer, followed by a current booster. The 555 timer, which is set to have a 50% duty cycle, controls the

duration of the rotation in one direction until a reversal occurs. The specific duration can be adjusted with the potentiometer. The purpose of the current booster is to increase the output of the 555 timer so that it can effectively trigger the relays that control the motors used for rotation (the relays are not shown in the diagram).

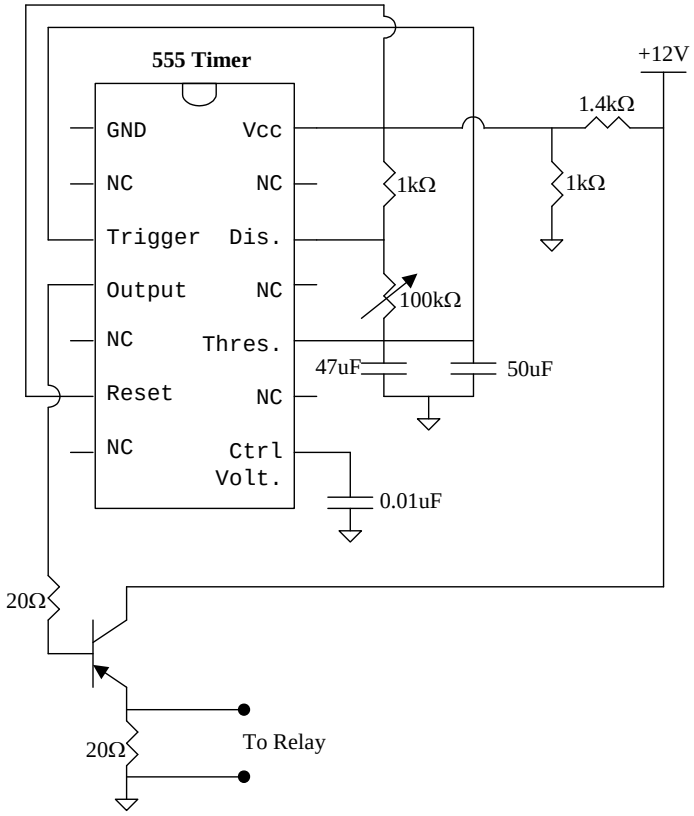

Figure 9 - Schematic of the reversal circuit

Film series 107-111 were grown using the reversal circuit. These films were grown at rotation rate of 100 rpm at 760 ºC. Film 112 was grown without the rotation reversal but at an additional 5 degrees undercooling temperature. Table 5 shows the number of rotations per each reversal used for the growth of each film.

Film	Undercooling Temp. (ºC)	rotation/ reversal	Reversal Period (sec)	Mismatch (Å)	Faraday Rotation (deg/μm)
UMD107	50	2	1.2	0.00278	1.22
UMD108	50	3	1.8	0.00239	1.28
UMD109	50	4	2.4	0.00239	1.20
UMD110	50	4	2.4	0.00241	1.24
UMD111	50	5	3.0	0.00237	1.16
UMD101	50	->inf	->inf	0.00234	1.26
UMD112	55	->inf	->inf	0.00378	1.25

Table 5 - Mismatch and specific Faraday rotation of films grown with rotation reversal.

As can be seen from Table 5, as the reversal period decreases, the magnitude of the mismatch increases. This means that more bismuth is incorporated into the film, and thus the film is in compression. Also, as this reversal period is increased, the mismatch asymptotically approaches the value for an infinite reversal period (UMD101). In addition, Table 5 indicates that the Faraday rotation of the films does not correlate to the period of rotation. Since x-ray diffraction results do predict a correlation between these two parameters, it can be hypothesized that the optical measurements for Faraday rotation are inaccurate. This hypothesis is justified because x-ray diffraction is known to produce very precise and accurate measurements for lattice mismatch. The discrepancy between the x-ray and optical measurements maybe due to the fact that some of the films that were grown are double layered instead of single layered, thus accounting for higher Faraday rotation.

As previously mentioned, as the reversal period increases, the value of the mismatch asymptotically approaches a constant value. This value correlates to the mismatch of films grown without rotation reversal. The trend is depicted in Figure 10. In

addition to the asymptotic behavior of the mismatch, Figure 10 also shows that this mismatch dramatically increases once the reversal period approaches one rotation per reversal.

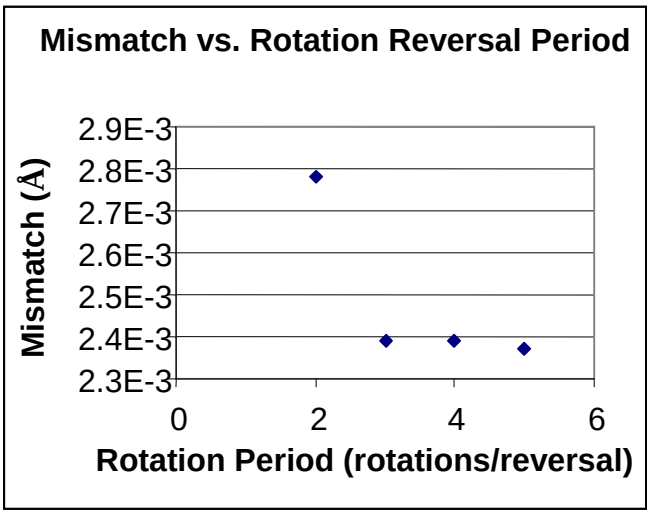

Figure 10 - Lattice mismatch versus the rotation reversal period. The error bar on this graph is ±0.00003 Å.

Three additional films were grown using melt UMD40, but with larger lattice substrates. The GGG substrates used to grow these three films had a lattice of approximately 12.48 Å. The lattice mismatch of these films is shown in Table 6. From this, it can be seen that the lattice mismatch is negative. This indicates that the films are in tension, and thus more bismuth needs to be incorporated into them.

Film	Undercooling (C)	Mismatch (Å)
UMD113	-50 º	-0.01831
UMD114	-75 º	-0.01188
UMD117	-90 º	-0.00584

Table 6-Mismatch of films grown with large lattice substrates

Figure 11 depicts a graph of the mismatch vs. the undercooling temperature for films UMD113, UMD114, and UMD117. The points of this graph have been fitted in order to determine the undercooling temperature at which the mismatch is equal to zero. Specifically, it is shown that an undercooling temperature of approximately 120 º C is required to grow matched films. However, it is difficult to maintain a stable melt at such a high cooling temperature.

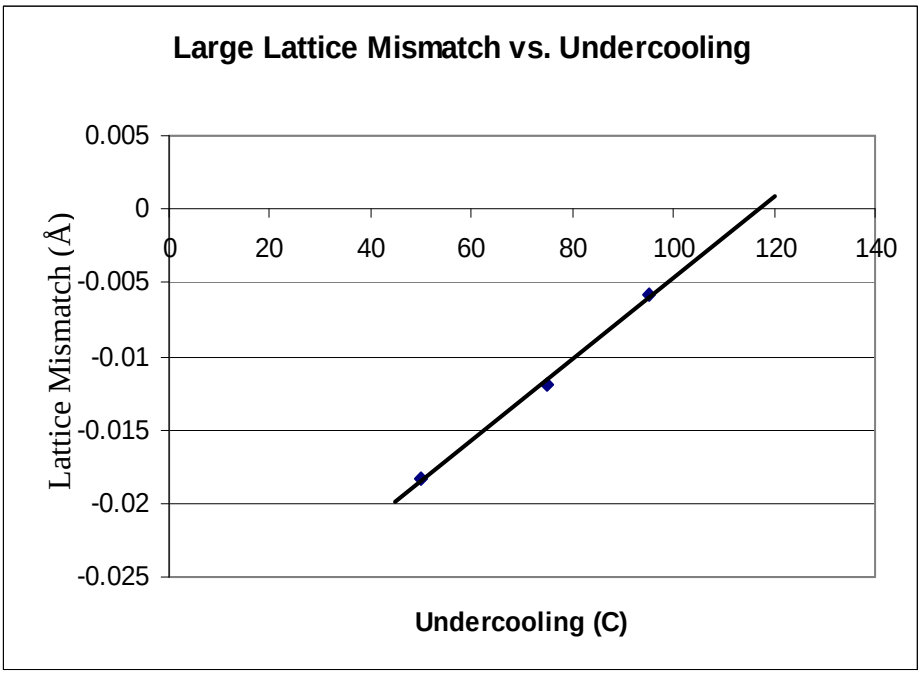

Figure 11 - Large lattice mismatch vs. undercooling temperature

Some ways to increase the bismuth content without going to higher undercooling temperatures are to increase the garnet to flux ratio or to increase the rotation rate of the substrate during film growth. However, increasing the garnet to flux ratio would create instabilities within the melt. In addition, this increased bismuth content will increase the lattice mismatch between the film and the regular sized GGG substrate (a=12.38 Å).

Thus, the use of a larger lattice will be required. The large lattice GGG substrate that is currently available has a lattice constant of approximately 12.48 Å. With current growth conditions, the amount of bismuth that can be incorporated into the film is approximately 0.8 formula units. However, more than 1 formula unit would be required to match the lattice of the film to the large lattice GGG substrate.

One way to reduce the lattice mismatch between the film and the larger lattice GGG substrate is to use a different rare-earth element in the film composition. Since the lutetium that is currently in the film has the smallest ionic radius (a=112.5 pm) of all of the rare-earth elements, it does not match well with the relatively large ionic radius of bismuth. The selection of a rare-earth element that has a larger ionic radius would decrease the mismatch between the film lattice and the GGG substrate lattice. Also, depending on the rare-earth element that is used to replace the lutetium in the melt, the uniaxial anisotropy and the magneto-crystalline anisotropy may be reduced.

Gallium Dilution

The addition of gallium to the melt affects many properties in the garnet film. Gallium, which is a diamagnetic ion, changes the anisotropy and saturation field of the film, which determines the magnetic sensitivity of the MOI. Gallium reduces the saturation magnetization of the film but it also reduces the Faraday rotation. This limits the amount of gallium that can be incorporated into the film. Lowering the saturation magnetization decreases the saturation field. Since the films are planar in magnetization, increasing the gallium content effectively increases the susceptibility of the film [5]. Typically the tetrahedral site is doped with gallium or other diamagnetic elements such as

aluminum in order to reduce the saturation magnetization [3]. Gallium and iron compete for the doping sites. Due to this, introducing gallium into the melt decreases the incorporation of iron into the film.

The growth-induced anisotropy is also affected by the diamagnetic ion doping [3]. Table 7 provides data demonstrating the effect of the gallium doping on growth-induced anisotropy. As seen from this table, an increase in the gallium content in the film corresponds to a decrease in the magnitude of the growth-induced anisotropy, K_g. The gallium doping also affects the magneto-crystalline anisotropy. Specifically, an increase in the gallium content corresponds to an increase in the magnitude of the magneto-crystalline anisotropy, K_1.

There is another limitation to increasing the gallium content in the film. A transition point during the growth process between achieving in-plane magnetization versus perpendicular magnetization in the film occurs as the concentration of gallium is increased [3]. The maximum gallium content in the film must be below 1 formula unit in order to grow in-plane films [3]. Although the gallium incorporation can be increased at higher undercooling temperatures, the degree of undercooling is limited because increased undercooling also increases the bismuth content. This high bismuth content would create a large lattice mismatch, which would result in out of plane magnetization. Thus, the amount of gallium that could have been incorporated would have been even less than predicated.

C_{Ga} (± 10%) (a/fu)	K_g (± 10%) (10^3 erg/cm^3)	K_1 (± 25%) (10^3 erg/cm^3)
0	69	-6.0
0.23	60	-4.3
0.47	55	-3.8
0.66	47	-2.7
0.84	33	-1.7
0.98	30	-0.8
1.10	26	-0.2

Table 7 - Variation of K_g and K_1 to Ga doping [4].

Chapter 3 - Ferromagnetic Resonance:

Basic Principles of FMR:

Ferromagnetic resonance (FMR) refers to the strong absorption of energy from the RF transverse field when the frequency of the RF field is equal to that of either the electron spin moment precession or to the magnetization precession around an applied DC magnetic field [15]. At this resonance frequency, all spins are precessing in phase with each other within the material. This is also known as the Uniform Precession Mode (UPM).

FMR can be used to study the various anisotropy energies that are used to control the magnetization direction and magnetization dynamics in thin films. This includes studying the shape, magnetocrystalline, magnetostrictive, and surface-induced anisotropy energies within these thin magnetic films as well as the interactions between magnetic layers.

In the presence of an external DC magnetic field, the mechanical and magnetic moments of the electron cause the magnetization vector to precess around the magnetic field lines as is shown in Figure 12a. This precession is induced by a torque that aligns the magnetic moment of the free electron to the external magnetic field $\vec{H}$. This torque can be expressed as

$$\vec{T} = \vec{M} \times \mu_0 \vec{H} \tag{24}$$

where μ_0 is the permeability of free space. This torque can also be related to the change in the total angular momentum of the electron, $\vec{J}$, over time by

$$\vec{T} = \frac{d\vec{J}}{dt} \tag{25}$$

It is also known that the total angular momentum of a electron can be related to its magnetic moment by:

$$\vec{\mu} = \gamma_0 \hbar \vec{J} = -g\mu_B \vec{J} \tag{26}$$

where $\gamma_0 = g\vec{\mu}_B/\hbar$ is the gyromagnetic ratio, μ_B ($\mu_B = q\hbar/2m_e \approx 9.27 \cdot 10^{-24}$ J/T) is the Bohr magneton, and g is the spectroscopic splitting factor, also known as the Landé factor, which is defined as $g\mu_B = -\gamma\hbar$. If (26) and (25) are substituted into (24), it follows that

$$\frac{d\vec{\mu}}{dt} = \gamma_0(\vec{\mu} \times \vec{H}) \tag{27}$$

Since $d\vec{\mu}$ is perpendicular to the ($\vec{\mu}$, $\vec{H}$) plane, $\vec{\mu}$ circumvents the $\vec{H}$ field in the direction that is determined by the right hand rule. The velocity at the top point of the μ_B vector is

$$v = \left|\frac{d\vec{\mu}}{dt}\right| = \gamma_0 H\mu \sin\theta \tag{28}$$

where θ is the angle between $\vec{H}$ and $\vec{\mu}$.

Using $R = \mu \sin\theta$ as the radius of the circle, and substituting *R* in the velocity equation, the frequency of the natural precession of $\vec{\mu}$ around $\vec{H}$ is

$$\omega_0 = \frac{\upsilon}{R} = \gamma_0 H \tag{29}$$

Since the gyromagnetic ratio, γ_0, is a constant, it is clear that the precession frequency, ω, is directly proportional to the magnitude of the magnetic field, $\vec{H}$.

When the electron spins are aligned, the total magnetization is

$$M = N\mu_B \tag{30}$$

where *N* is the number of uncompensated electrons spins per unit volume in the system. The dynamics of the magnetization vector can be described by using the classical equation of motion

$$\frac{d\vec{M}}{dt} = -\gamma(\vec{M}x\vec{H}_{eff}) \tag{31}$$

The magnetic field, $\vec{H}_{eff}$, in this equation is the sum of all magnetic fields that effect the system. When an RF field is applied perpendicularly to the DC field, the total magnetic field will include an alternating field term. Thus, the total magnetic field can be stated as as

$$\vec{H}_{eff} = \vec{H}_{\mathbf{0}}^{\,eff} + \vec{h}e^{j\omega t} \tag{32}$$

where $\vec{h}e^{j\omega t}$ RF component of the magnetic field, and $\vec{H}_{\mathbf{0}}^{\,eff}$ is the effective DC field within the material. This effective DC field term includes the external DC field, the effect of any anisotropies that may be present in the material, and the shape anisotropy field. The system absorbs small amounts of energy from this RF field at all frequencies. However, when the frequency of the RF field is equal to the natural frequency of the precession of the electron moment, the amount of energy absorbed from the RF field increases dramatically. The absorption of energy from the RF field increases the radial

amplitude of the precession of the magnetic moment around the DC magnetic field. This is shown in Figure 12b.

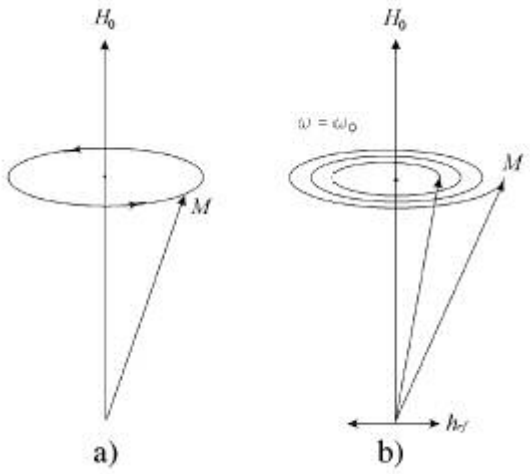

Figure 12 - Precession of magnetization vector $\vec{M}$ in (a) a constant magnetic field, (b) an alternating magnetic field whose frequency is near the natural precession frequency [7].

The amplitude of the precession is limited by damping. A damping term can introduced into (31), which results in

$$\frac{d\vec{M}}{dt} = -\gamma(\vec{M}x\vec{H}_{eff}) - \frac{\lambda}{\left|M^2\right|}\vec{M}x(\vec{M}x\vec{H}_{eff}) \tag{33}$$

This damping term acts as a torque that reduces the precession angle. The above equation is known as the Landau-Lifshitz equation [12].

The magnetization vector can also be represented as the sum of a DC term and an alternating term

$$\vec{M} = \vec{M}_0 + \vec{m}e^{j\omega t} \tag{34}$$

The solution of (33) can be found by using the small signal approximations $h << H_0^{eff}$ and $m << M_0$. Also, by using a linear approximation of (33), the damping term can be neglected. Furthermore, (33) can be separated into two terms, a DC term and an AC term. The DC term of this equation can be expressed as

$$\gamma(\vec{M}_0 x \vec{H}_0^{eff}) = \mathbf{0} \tag{35}$$

This shows that, in the case of an isotropic ferromagnet, the DC component of the magnetization will be aligned parallel to the effective DC field. The AC equation is written as

$$j\omega\vec{m} = \gamma(\vec{M}_0 x \vec{h} + \vec{m} x \vec{H}_0^{eff}) \tag{36}$$

Using the conventions that $\vec{H}_0^{eff}$ and $\vec{M}_0$ are along the z-direction, and that the RF field is applied in the x-direction, (36) can be expanded to the following set of coupled equations

$$\begin{aligned} j\omega m_x + \gamma H_0^{eff} m_y &= \gamma M_0 h_y \\ -\gamma H_0^{eff} m_x + j\omega m_y &= -\gamma M_0 h_x \\ j\omega m_z &= \mathbf{0} \end{aligned} \tag{37}$$

Solving these coupled equations for *m* results in

$$\begin{aligned} m_x &= \frac{\gamma M_0(\omega_0 h_x + j\omega h_y)}{(\omega_0^2 - \omega^2)} \\ m_y &= \frac{\gamma M_0(-j\omega h_x + j\omega_0 h_y)}{(\omega_0^2 - \omega^2)} \\ m_z &= \mathbf{0} \end{aligned} \tag{38}$$

where ω_0 is the ferromagnetic resonance frequency of the electron spin in a ferromagnetic material.

The demagnetization coefficients for a uniform thin-film are N_x, N_y, and N_z, where $N_x=N_y=0$, and $N_z=4\pi$. In this case, when a magnetic field is applied perpendicular to the plane of the thin-film, the resonance frequency can be expressed as

$$\omega_0 = \gamma(H_0^{eff} - 4\pi M_s) \tag{39}$$

Conversely, in the case where the applied field is parallel to the film plane, the resonance frequency becomes

$$\omega_0 = \gamma\sqrt{(H_0^{eff}(H_0^{eff} + 4\pi M_s)} \tag{40}$$

The DC effective field can be expressed using the uniaxial anisotropy and the demagnetization field of the film, as

$$H_0^{eff} = \frac{2K_u}{M_s} - 4\pi M_s + H_0 \tag{41}$$

where K_u is the constant of uniaxial anisotropy. Thus (39) can be rewritten as

$$\omega_0 = \gamma(H_0 + \frac{2K_u}{M_s} - 4\pi M_s) \tag{42}$$

for the case of a perpendicular applied magnetic field. Also, using (41), equation (40) can be rewritten as

$$\omega_0 = \gamma\sqrt{(H_0(H_0 - \frac{2K_u}{M_s} + 4\pi M_s)} \tag{43}$$

for the case of a parallel applied magnetic field.

The equations (42) and (43) are only valid when the magnetocrystalline anisotropy is much smaller than $4\pi M_s$. When this is not the case, the expression for the resonance frequency can be found by using the Smith-Suhl formula [7]

$$\left(\frac{\omega}{\gamma}\right)^2 = \frac{1}{M_s^2 \sin^2(\theta_M)}\left(\frac{\partial^2 f}{\partial \theta_M^2}\frac{\partial^2 f}{\partial \theta_M \partial \varphi_M} - \left(\frac{\partial^2 f}{\partial \theta_M \partial \varphi_M}\right)^2\right) \tag{44}$$

In this equation f is the total free energy density of the system, and θ and φ are the polar and azimuthal angles of the magnetization.

For the (100) films, the free energy that corresponds to the crystalline anisotropy can be expressed as

$$f_{ani} = K_1(\cos^2\theta\sin^2\theta + \sin^4\theta\cos^2\varphi\sin^2\varphi) \tag{45}$$

As a result, the following equations can be used to relate the magnetic fields and the gyromagnetic ratios to the resonant frequency of the (100) films

$$\begin{aligned}
\omega &= \gamma(H_1 + H_{Ku} - 4\pi M_s + H_{K1}) \\
\omega^2 &= \gamma^2(H_2 - H_{Ku} + 4\pi M_s + H_{K1})(H_2 + H_{K1}) \\
\omega^2 &= \gamma^2(H_3 - H_{Ku} + 4\pi M_s - H_{K1})(H_3 + \frac{H_{K1}}{2})
\end{aligned} \tag{46}$$

where H_1, H_2, and H_3 are the resonant field values for the magnetic field vectors that are parallel to the <100>, <010>, <011> crystalline directions, respectively. H_{Ku} is the uniaxial anisotropy field, and can be expressed as $2K_u/M_s$. H_{K1} is the crystalline anisotropy field, and can be expressed as $-\partial f_{ani}/\partial M_s$.

FMR Apparatus:

A standard microwave spectrometer with a wide-band non-resonant transmission stripline is used to perform the FMR measurements. The schematic of the FMR system used perform the measurements for this experiment is shown in Figure 13. A list of the equipment and components that are used in the experimental setup is shown in Appendix C. The system uses a phase-lock detection method in order to enhance the signal to noise ratio of the resonance signal. This system can support sample with sizes of up to 1 square inch. The sample is placed inside a minibox that is made out of a non-magnetic material, so that it will not perturb the magnetic field lines creates by the magnet. The schematic of this minibox is shown in Figure 14. A gold stripline is deposited on an alumina substrate that is resting on pedestals within the minibox. The sample is sandwiched between the top of the stripline and the bottom of the lid of the minibox. The lid of the minibox serves as the ground plane for the system. The RF signal generated by a microwave source is delivered to the minibox via a circulator. The incident signal is reflected by a short at the opposite end of the stripline. The reflected signal is then directed to a diode detector by the circulator. The output of the diode detector is a DC voltage that is proportional to the power of the incident microwave signal.

The stripline is designed to match the 50-ohm impedance of the SMA connector and the 50-ohm impedance of the coaxial cables. Also, the stripline must support microwave signal frequencies ranging from 5 to 10 GHz. According to calculations performed with APPCAD 2.0 [17], it was found that, in order to obtain this range of frequencies, the thickness of the 96% alumina substrate needed to be 42 mils, the thickness of stripline needed to be 2.1 mils and the width of the stripline needed to be 40

mils. Through simulations, it was found that, as a function of frequency, the characteristic impedance of the stripline varies between 48.9 and 49.8 ohms for the calculated dimensions, which is very close to the intended impedance of 50 ohms.

The FMR measurements are made by using a signal at a constant RF frequency and by varying the applied DC magnetic field. This choice of methods is to avoid second order frequency response changes within the stripline when a signal with a varying RF frequency is applied. A DC power source is used to generate a slowly-varying DC current that is fed to the magnets. This generates a magnetic field that is detected using a Hall effect based gaussmeter. Since the level of energy absorption of the system is weak, an additional small modulated magnetic field is added on top of the DC field. This AC field has a frequency of 100Hz, and a peak-to-peak amplitude of 2 Oe. The modulation of the signal allows for the detected signal to be amplified with a lock-in amplifier. The output of this lock-in amplifier is effectively the derivative of the actual signal absorption.

The DC power source, gauss meter, and lock-in amplifier are all controlled via a LABVIEW program. A diagram of this LABVIEW program is shown in Appendix D.

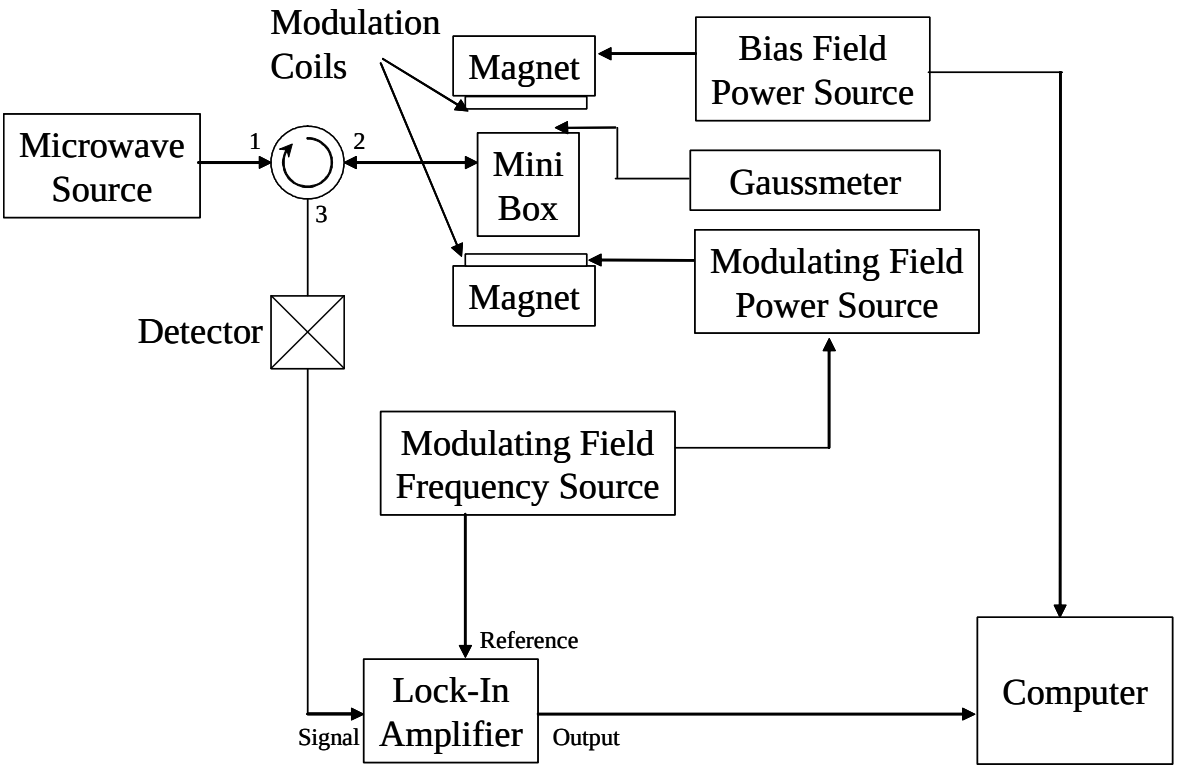

Figure 13 - Schematic of a wideband spectrometer FMR system

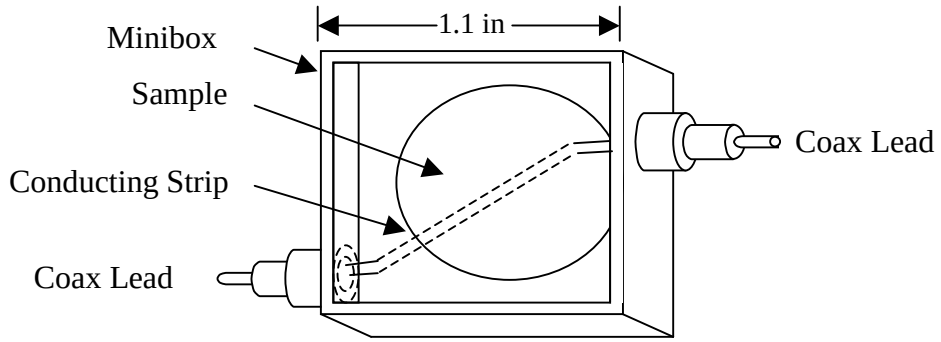

Figure 14 - Schematic of minibox

Determination of Cubic and Uniaxial magnetic Anisotropy Using FMR:

The FMR spectrometer system described above has been used to determine the cubic and uniaxial anisotropy constants, and the gyromagnetic ratio of the bismuth iron

garnet films grown with the LPE furnace described in Chapter 2. Multiple angular measurements are needed in order to determine the values of the uniaxial and cubic magnetic anisotropy constants. The macroscopic expressions for the energy of uniaxial and cubic magnetic anisotropy; and of the demagnetization energy (given in (46)) are used to derive the constants. The equilibrium orientation of the magnetization vector in external magnetic field is aligned to the (100) plane. The direction of the easy axes of the magnetization vector has been determined by using the method described in [18]. In this method, the optical response of the samples is measured while they are under the action of a rotating magnetic field, which in turn allows for the identification of the crystallographic axes.

The dependence of the resonance field, H_{res}, was measured as a function of the angle, θ between the applied DC field and the <100> direction. The shape of the H_{res} versus θ is dependent on the demagnetization field, magnetocrystalline and uniaxial anisotropies. When the gyromagnetic ratio, RF frequency, and the DC resonance field are known, the data can be fitted to determine the K_1, K_u, and $4\pi Ms$ parameter.

Using the method described in [19], the $\frac{K_u^*}{M_s} = \frac{K_u - 2\pi M_s^2}{M_s}$ of film 102 was measured. This sample was grown on a (100) substrate and optical characterization shows that it has planar magnetization. The angle of the sample with respect to the field direction was varied in 10 degrees increments. The observed resonance field shifts to higher values as the angle is varied. Figure 15 shows this change in the DC resonance field as the angle at which the magnetic field is applied to the sample is varied. The fitting is done not for the DC resonance field but for the quantity

$\frac{\omega}{\gamma} - H_{DC} = \frac{K_u^*}{M_s}\frac{\mathbf{1}}{\mathbf{2}}\left(\mathbf{1} + \mathbf{3}\cos \mathbf{2}\theta_H\right)$. The result of this fitting is $\frac{\mathbf{2}K_u^*}{M_s} = -\mathbf{1520}G$, which is comparable with films of similar composition [20].

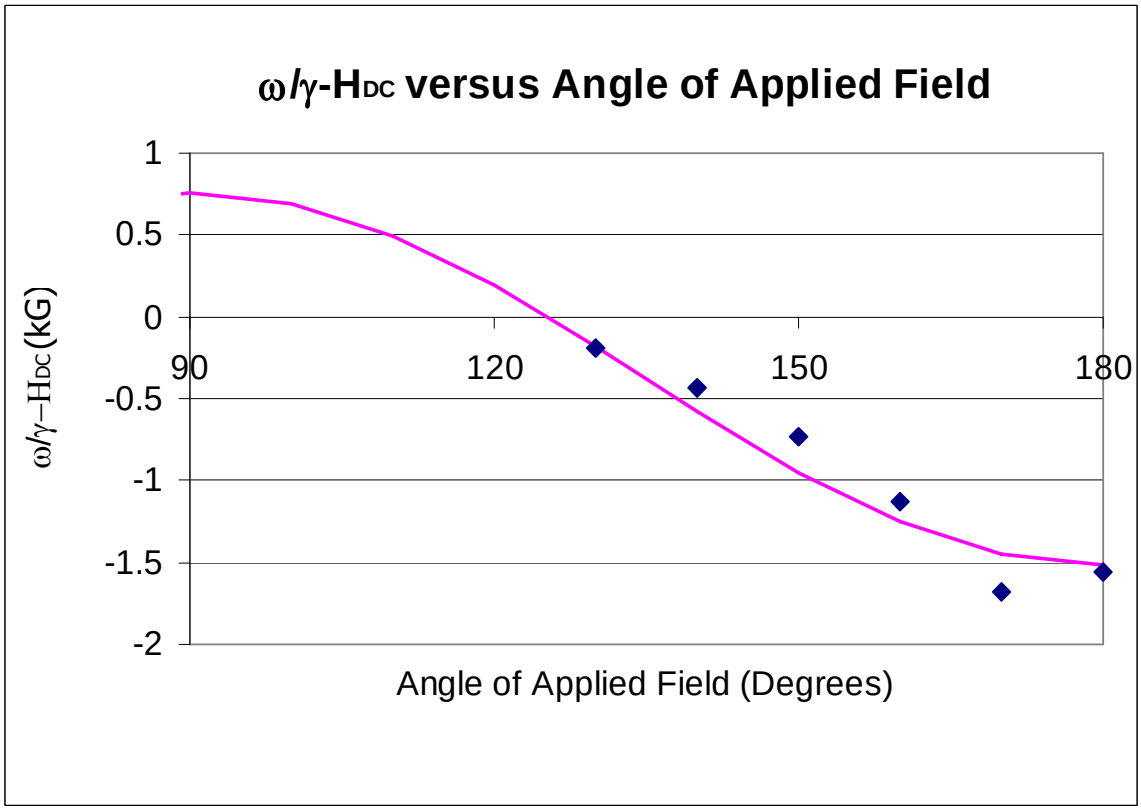

Figure 15 – Determination of magnetic uniaxial anisotropy constant for a magnetic garnet epitaxial film using ferromagnetic resonance. The data was fitted using the method in [19]

Determination of Gyromagnetic Ratio

The gyromagnetic ratio, γ is determined by measuring the resonance field at different frequencies. From (46), it can be seen that the resonance field is directly proportional to the resonance frequency through the gyromagnetic ratio. Figure 16 shows the shift in the resonance field as the frequency is varied, for film 74. The gyromagnetic

ratio is then determined by interpolating the data from Figure 16. Table 8 lists the measured gyromagnetic ratios for the films that were studied.

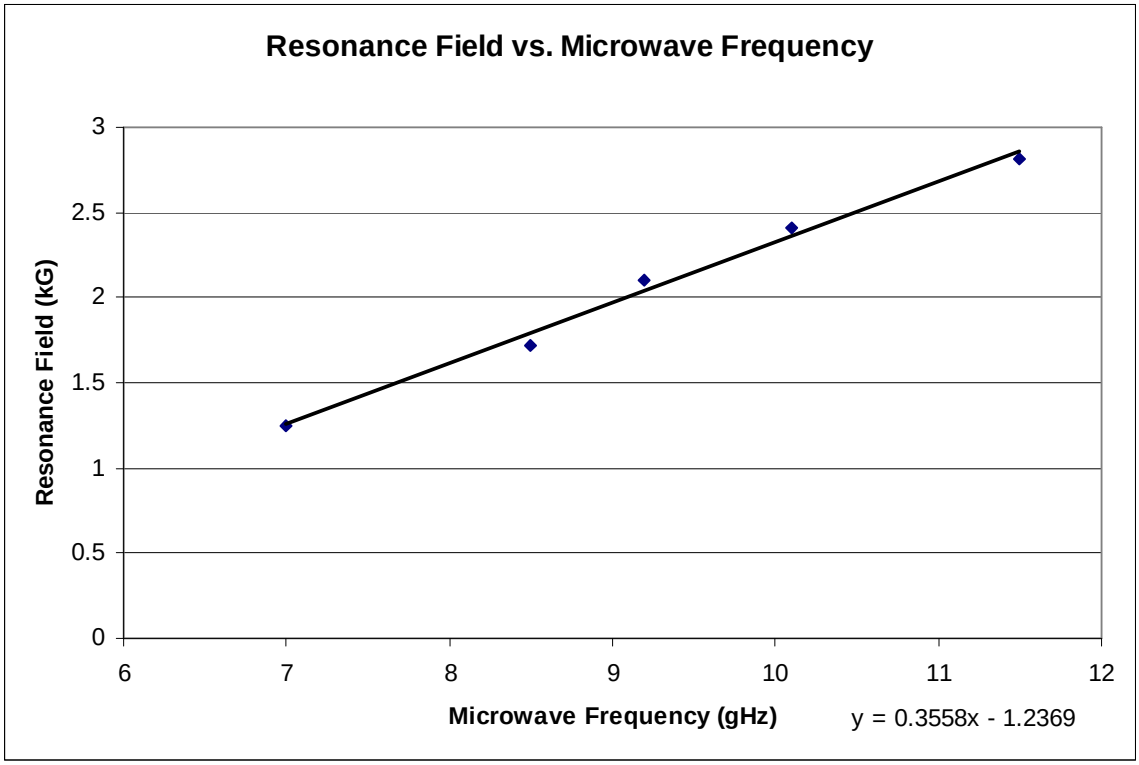

Figure 16 - Changes in resonance field as the frequency is varied for film 74

Melt	Film	Gyromagnetic Ratio (GHz/kG)
UMD31	UMD70	2.978
UMD31	UMD74	2.81
UMD40	UMD 90	3.077
UMD40	UMD111	3.125

Table 8 – Gyromagnetic Ratios of the films studied

Magnetostatic waves

Magnetostatic waves were observed in the FMR measurements of the films as additional absorption peaks. These waves are excited in the stripline in the form of static

spin oscillations. The orientation of the external magnetic field with respect to the sample determines whether the waves will propagate at the surface or in the volume of the sample [3]. The amplitude of these waves increases with the intensity of the microwave signal. Additionally, the amplitude of these waves decreases with increasing DC field, due to a decrease in the amplitude of the spin's precession. A typical absorption curve for a sample that exhibits spin wave resonances is depicted in Figure 17. When the applied field reaches the resonance value, the amplitude of the precession motion increases. This enhances the coupling of the spin waves with the RF magnetic field. The result of this is the appearance of a "ringing effect" that can be seen on the absorption curve. Every absorption peak of this ringing corresponds to a different magnetostatic mode.

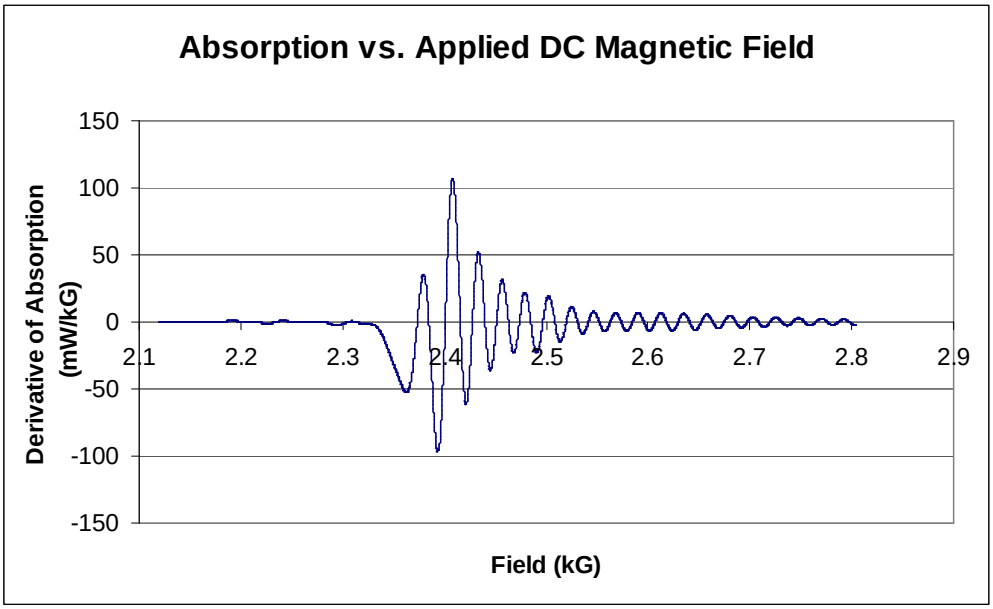

Figure 17 - Example of ringing effect demonstrating magnetostatic waves for film 74

Chapter 4 - Applications of Magneto-optical Indicator Films

The response of bismuth iron garnet films to magnetic fields makes them useful for a large number of applications involving magnetic field detection. One such application is the detection of the current inside superconducting samples. For this, the garnet films are used to visualize the stray magnetic fields of the superconductors [2]. Vortices inside the superconductors can also be imaged by using these garnet thin-films. In addition, non-destructive evaluations of micro-cracks and surface defects in conducting materials have been accomplished using both in-plane and perpendicular magnetization Bi-doped iron garnet thin-films [3]. For this investigation, the bismuth iron garnet thin-films that were grown and characterized, as described in the previous two chapters, have been used for the forensic analysis of magnetic tapes.

A magneto-optical indicator utilizes the Faraday effect to visualize the magnetic field patterns that are recorded on a magnetic media. This process is depicted in Figure 18. In this figure, linearly polarized light is transmitted through a polarizer and directed onto the MOI film. When there is no external magnetic field, the magnetization of the garnet film is parallel to the plane of the film. Figure 19 shows the perpendicular component of the magnetic perturbation on the media. The component of this perturbation that is normal to the film plane in turn gives the magnetization vector a normal component. This normal component of the magnetization vector causes a Faraday rotation of the linearly polarized light. The light beam is reflected off of the mirrored surface at the lower surface of the film and is retransmitted through the film. As previously mentioned, the angle of rotation is doubled through this process, since the Faraday effect is a non-reciprocal process. The polarization of the reflected light beam is

then measured with a polarization analyzer. The polarization analyzer detects the Faraday rotation, and thus the magnetic field distribution inside the indicator film is displayed as an image of bright and dark tones. These tones effectively map the local changes of the magnetic inductance, $\vec{B}$.

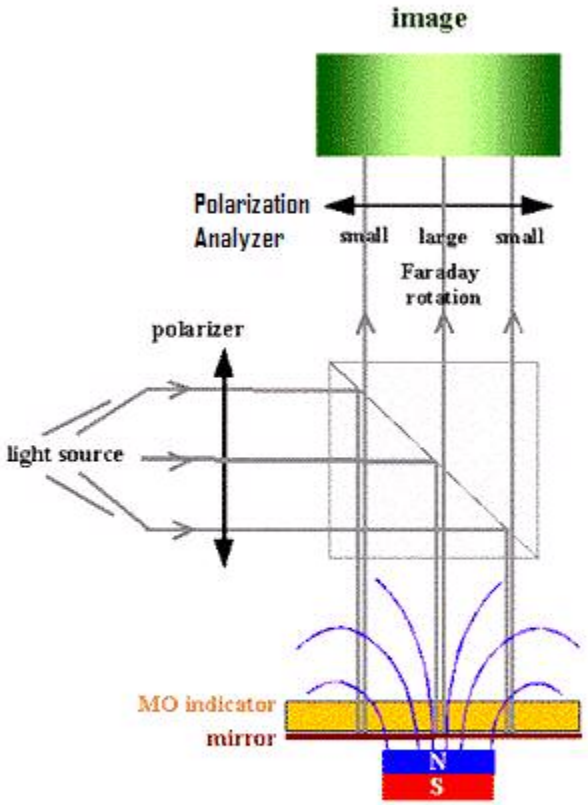

Figure 18- Diagram of MOI system [8].

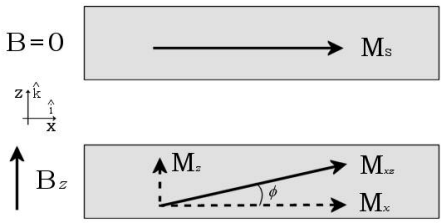

Figure 19 - Magnetization vector in the film with and without the presence of external field [8].

Previous work has been done to view the distinctive features on audio magnetic media. This work focused on the use of magnetic particle suspension via a chemical solution in order to image the audio tracks [16]. For this process, the solution must be prepared, applied to the tape, and allowed to dry before the magnetic field patterns on the audio tapes can be imaged [16]. These field patterns are used to describe many recording events, such as the 'start' and 'stop' events, as well as event overrecordings. Figure 20 shows an image of an audio tape. In this image, the field patterns represent the audio track information. The information on the audio tapes is then compared with known recording patterns in order to determine if the tapes have been tampered with.

The magnetic garnet indicator films developed in this project serve as a replacement for the magnetic particle suspension. The garnet film has intrinsic properties that produce non-contaminating results for the magnetic field patterns [16]. The transition of the magnetization vector in the magnetic tape is mapped with the garnet film. The linear field response of the garnet to the magnetic field patterns is converted to a visual gray scale image [16]. The garnets grown in this study are tailored to be highly sensitive, and to provide high spatial resolution images, making them ideal for forensic analyses.

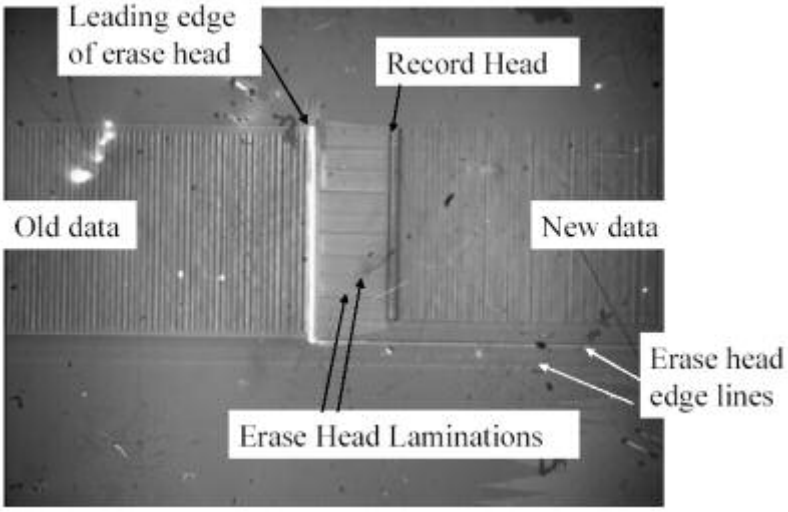

Figure 20 - Image of magnetic tape recording with erase head information [14].

Imager System

For this study, an imager system has been developed to provide a complete analytical tool that can be used to view and save recordings on magnetic media. This system will be used for routine forensic examinations. The garnet imager system has the ability to obtain low magnification images of the recordings without compromising a large a field of view, while still maintaining the ability to achieve submicron resolution. An ideal garnet for magneto-optical imaging should have good sensitivity (from ~1 Oe to ~15 Oe) and have a linear response to the fields that are produced by the magnetic sample [16]. These garnets should also be designed to precisely replicate the field distribution in the media while producing a minimal amount of artifacts. Some garnet artifacts that are possible include planar domain walls, serpentine domain walls, scratches, and growth defects. Planar and serpentine domain walls are classified as artifacts because they are

not directly associated with the magnetization pattern in the tape. Perpendicular serpentine walls are of less concern because they can be avoided by using planar magnetization films. High Faraday rotation in the garnet is also desirable in order to have stronger contrast of the magnetic patterns.

The main components in the design of the garnet imager system stage are the field of view, the area of magnetic tape under the garnet, and the area of interest for examination. The field of view is determined the by the microscope objective and by the optical features of the camera. The field of view can range from tens of microns to several millimeters. The design allows for one square centimeter of observable tape area under a piece of garnet. The observable area of this tape is limited by the size of the garnet sample. Larger garnet samples are impractical due to the lack of uniform contact between the magnetic tape and the garnet. The examination area is typically tens of square millimeters or larger depending on the features observed.

The main concern when capturing the magnetic pattern is the spatial relationship between the various recording events. The design of this system allows for the tape to slide underneath the garnet. This allows the examiner to make measurements on areas of the tape that are outside the region of the mounted garnet. However, due to this ability, a method for tracking the position of the event relative to the field of view is required. Thus, a linear encoder system is incorporated into the stage design to track the movement of the features on the tape.

Components of Imager System

The apparatus of the imager system includes a polarized light source, a microscope, a digital camera, a set of linear encoders, and a computer control system. The schematic of this imager system is depicted in Figure 21, and the equipment that is used in this setup is listed in Appendix E. A polarized light microscope that is equipped with both tungsten filament and mercury arc lamp light sources is used to view the field patterns. The level of magnification of the microscope objectives can be varied from 2.5X to 50X. A monochrome digital video camera is used for obtaining high-resolution, grayscale real-time images. The resolution of these images is 1.2 million pixels with an image depth of either 8 bits or 12 bits per pixel (selectable by the user). A pair of linear encoders that is attached to the microscope stage measures the horizontal and vertical stage position. For this project, a control box was built to deliver the output of the linear encoders to a computer controlled counter card. The schematic of the control box is shown in Figure 22. This counter card is used to determine the position of the stage with respect to the reference point.

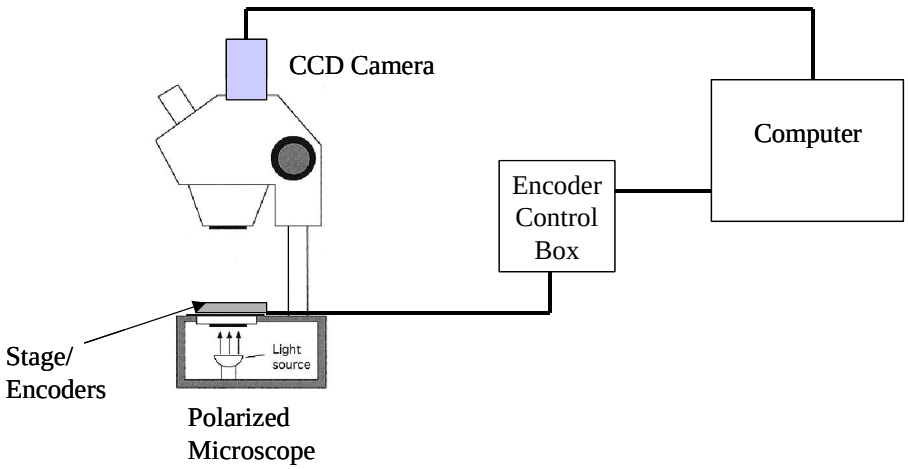

Figure 21 - Schematic of the Imager System.

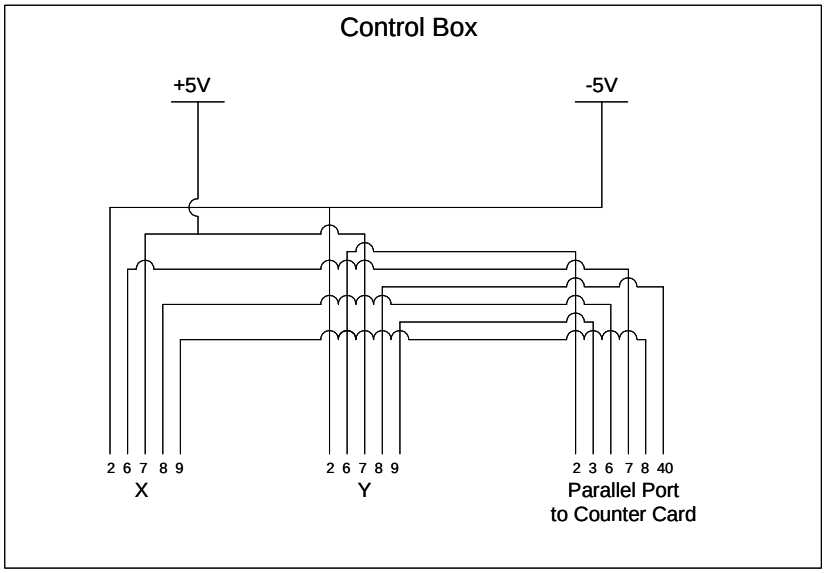

Figure 22 – Schematic of control box

The stage has two slots on either side of the central aperture that are used to align the tape. These slots are necessary since the reflective coating of the garnet normally blocks the transmission of light through the tape [16]. A photo of this stage is depicted in Figure 23. The top plate of the stage is leveled by two "set screws" on either side of the top plate. Since the distance between the objective and the garnet is small, a recessed area on top of the garnet is provided in order to allow for a greater work area [16]. An embedded ruler on the stage determines the position of the garnet holder [16]. Movable clamps on the front of the holder press the garnet firmly on the tape. This is depicted in Figure 24. These clamps are able to slide against the guide rail in order to maintain the alignment of the holder as the tape is moved along the garnet.

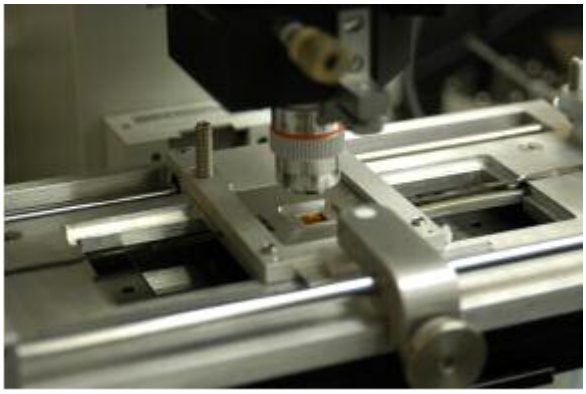

Figure 23 - Garnet Imager Stage [16]

A spring-loaded tape clamp is situated at either end of the stage. In normal operation, a length of tape is drawn out of its cartridge, placed onto the stage, and clamped into place [16]. The position of the left clamp is used as a reference point for all of the proceeding measurements.

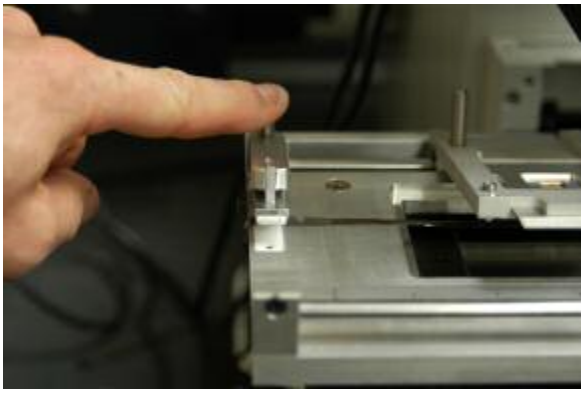

Figure 24 - Tape Clamp [16]

Software Interface of Imager System

The LABVIEW program that was developed for this imager system gives the user full control over the functions of the CCD camera. Since different images require different sets of camera parameters, having software control over the CCD camera functions greatly improves the efficiency of this imager system. In addition, the design of the graphical user interface for this LABVIEW program serves to provide the user easy access to the camera parameters. This user interface is depicted in Figure 25.

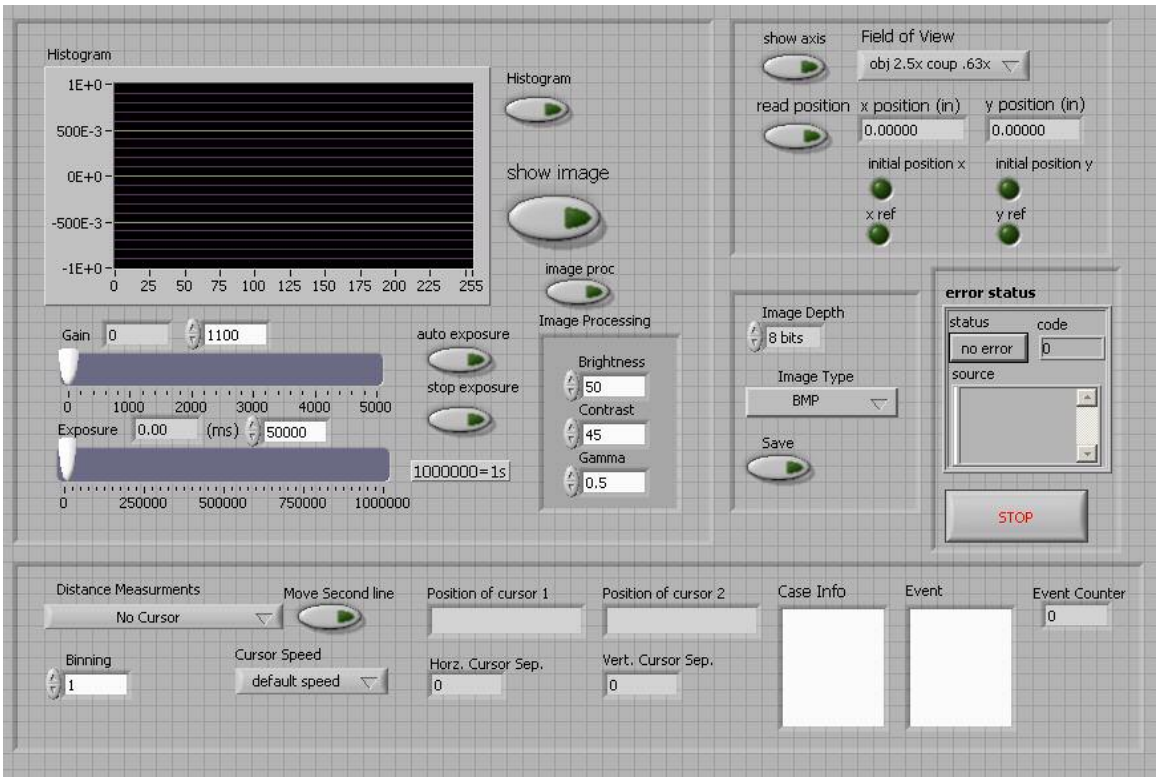

Figure 25 - Screen capture of the user interface of the LABVIEW imager program

One of the camera parameters that can be changed with this user interface is the image depth. The image depth is defined as the number of bits that represent each pixel

in the captured image. The CCD camera used for this imager system has the option of two depth sizes, 8 bits and 12 bits. For an 8-bit image depth, 8 bits are used to represent each grayscale pixel. Thus, 256 shades of gray are available for each pixel of the image. For a 12-bit image depth, 12 bits are used to represent each grayscale pixel. In this case, 4096 shades of gray are available for each pixel, resulting in an image of higher contrast and thus higher resolution. However, increasing the image depth also increases the file size. The file size of the 12-bit image is twice that of the 8-bits image. The image size does not increase proportionally to the bit size because the LABVIEW software can only process and save either 8-bit or 16-bit pixel grayscale images. For this reason, a 12-bit image that is recorded by the camera must be saved as a 16-bit image. In addition, the 12-bit image that is captured by the CCD camera is transmitted to the software as a matrix of unsigned integers. However, LABVIEW defines a 16-bit image as a matrix of signed integers. For this reason, all received bits must be converted from unsigned values to signed values and then scaled to 16 bits. This conversion has to be implemented in such a way as to allow for the image capture process to remain real-time. However, since this conversion adds processing time to the program, the program must be designed to run as efficiently as possible.

There are several other limitations when processing 16-bit images with LABVIEW. One such limitation is that LABVIEW does not display text on 16-bit images. In order to display horizontal and vertical scales, as well as user comments on the image, an 8-bit background image that includes this information must be created. This background image is then scaled from 8-bit to 16-bit. After this conversion, the background image is merged with the image that was captured from the CCD camera.

Once again, this process must be implemented in such a way as to allow for the image capture process to remain real-time.

Image Type	8 bits	12 bits
File size	1.71 MB	3.42 MB

Table 9 – File size of images with different pixel depth

Two other parameters that can be adjusted with the LABVIEW software are the exposure and gain of the camera. Although the software allows for a manual input of these parameters, an auto exposure function is also provided. This function automatically adjusts the gain and exposure of the camera in order to obtain a high quality image. The auto exposure algorithm is designed to maintain an upper and lower limit on the average number of pixels in the image that are saturated. Additionally, the front panel displays an active histogram of the image. Other parameters that can be manually adjusted with the LABVIEW program are the brightness, the contrast, and the gamma values.

By using the scales provided by the linear encoder, the user has the option to record the position of the magnetic signatures (events) on the tape and to document these events on the image. Distances between two events on the tape can also be determined from this method. This measurement is available by using the “cursor” option on the front panel. In addition to measuring the distance between two events, the horizontal and vertical position of single events, as well as the track width of the magnetic recordings, can be measured. A saved image of a cursor measurement between two events on a magnetic recording is displayed in Figure 26.

The software is also capable of providing the user with the ability to document the "case" and "event" details before saving the image. After all of the post-processing is complete, the user is able save the image, along with any required documentation, in both tiff and bitmap image formats.

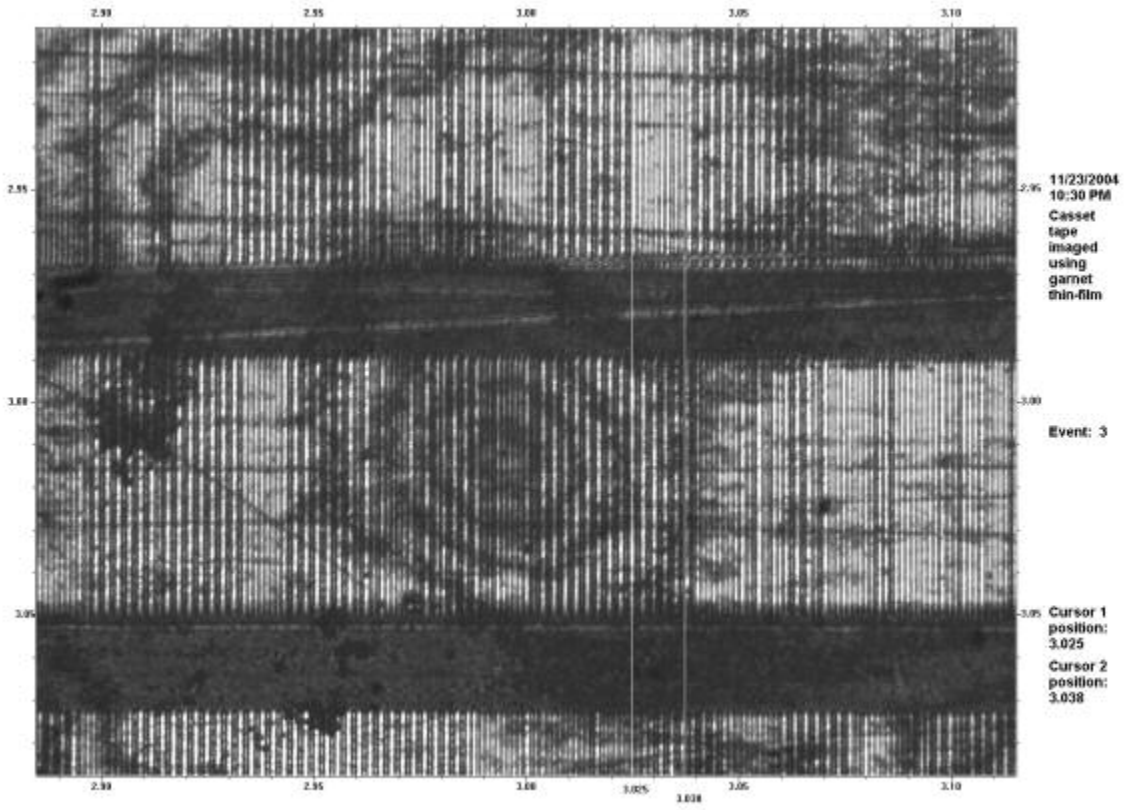

Figure 26 – Image of the magnetic information from a cassette tape that was recorded with the magnetic imaging system

Chapter 5 – Future Work

In the future, different melt compositions may be explored to enhance the magneto-optical properties of the Bi-doped iron garnet films. The goal of this would be to include more bismuth into the film. As stated in Chapter 2, an increase in the amount of bismuth will increase the specific faraday rotation of the film, making it more sensitive to magnetic field distributions. A proposed method to increase the bismuth content in the film is to increase the garnet to flux ratio. However, this increase would create instabilities within the melt. In addition, this increased bismuth content will increase the lattice mismatch between the film and the regular sized GGG substrate (a=1.238nm). Thus, the use of a larger lattice will be required. There is a larger lattice GGG substrate size that is currently available (a=1.248nm). With current growth conditions, the amount of bismuth that can be incorporated into the film is approximately 0.8 formula units. However, more than 1 formula unit would be required to match the lattice of the film to the large lattice GGG substrate.

One way to reduce the lattice mismatch between the film and the larger lattice GGG substrate is to use a different rare-earth element in the film composition. Since the lutetium that is currently in the film has the smallest ionic radius of all of the rare-earth elements, it does not match well with the relatively large ionic radius of bismuth. The selection of a rare-earth element that has a larger ionic radius would decrease the mismatch between the film lattice and the GGG substrate lattice. Also, depending on the rare-earth element that is used to replace the lutetium in the melt, the uniaxial anisotropy and the magneto-crystalline anisotropy may be reduced. From Table 2, it can be seen that ytterbium would be a suitable replacement for the lutetium. Since ytterbium when

coupled with bismuth has low K_g and K_1 values, the use of this element may reduce the uniaxial and magneto-crystalline anisotropies within the film.

In order to enhance the capabilities of the FMR characterization process, a new waveguide needs to be developed to transmit the microwave signal to the sample. Currently, the waveguide utilizes a stripline design, as was depicted in Figure 14. The disadvantage of this design is that it limits the transmission of the microwave signal at certain frequencies. In order to overcome this limitation, a coplanar waveguide needs to be developed. This waveguide would allow for the wideband transmission of the microwave signal (1GHz – 50GHz) to the sample.

Chapter 6 - Conclusion

Bismuth iron garnet thin-films can be used for magneto-optical imaging applications. These films are grown using the liquid phase epitaxy method, which produces single crystal, high quality films. The melt composition that is used to grow these garnets is selected in order to produce planar magnetization films with low magneto-crystalline and uniaxial anisotropies. Also, this melt composition is designed to incorporate more bismuth into the film, thereby increasing the specific Faraday rotation of the film. This effectively tailors the films to be highly sensitive to spatial magnetic field distributions. These garnet films are characterized by measuring their ferromagnetic resonance, which allows their magneto-crystalline and uniaxial anisotropies to be determined. An imager system that utilizes these garnet films has also been developed to visualize magnetic recording from cassette tapes. The Federal Bureau of Investigation (FBI) uses these captured images for forensic applications.

Appendix A - Diagram of Front Panel of Furnace Control

Software

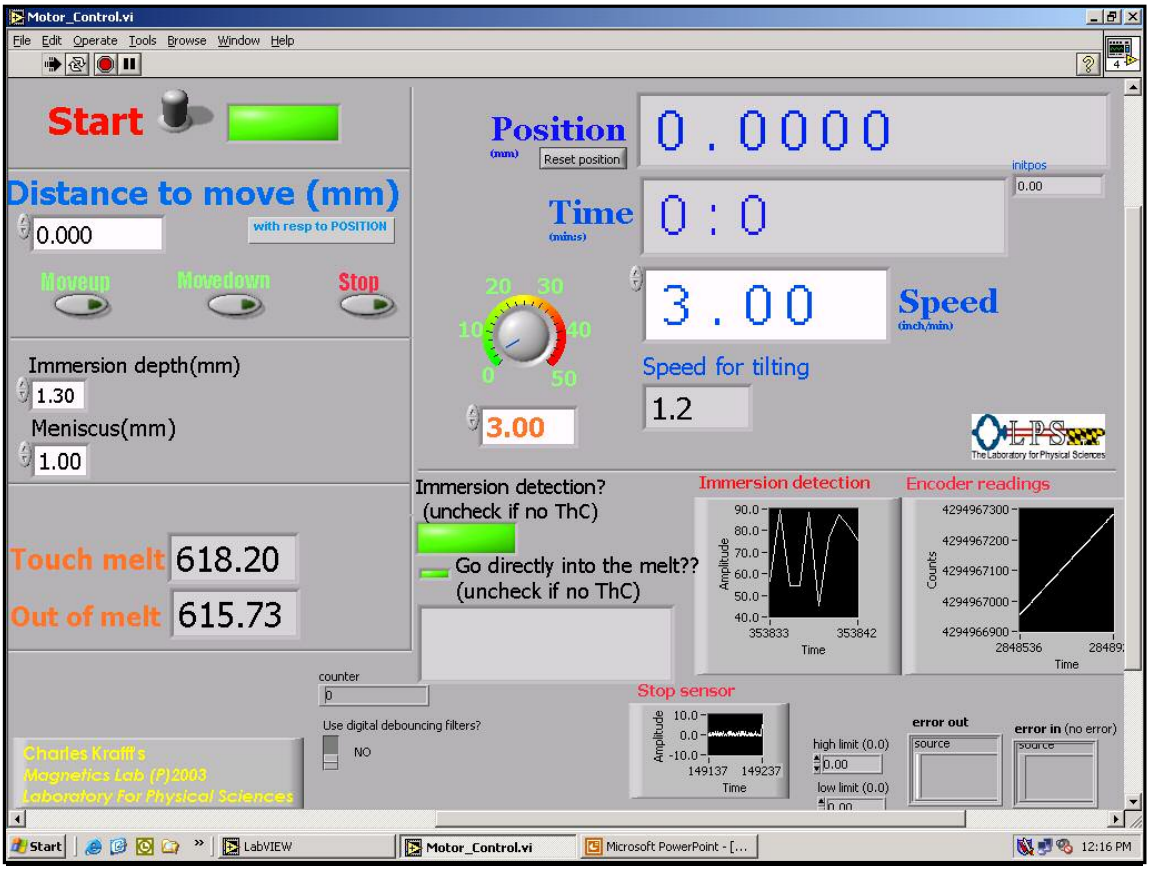

Appendix B - List of Equipment and Parts of Film Growth Process

1) National Instruments NI-SCXI-1000: Chassis
2) National Instruments NI-SCXI-1161: Relay Module
3) National Instruments NI-SCXI-1302: Connector Board
4) National Instruments PCI-6601: Counter Card
5) Omega Thermo-Couples
6) Applied Test System Inc. 3110: Tube Furnace - Max Temperature=1100 ºC
7) Spherosyn Digital Newall Linear Encoder

Appendix C - List of Parts of FMR Apparatus

1) Gigatronics Microwave Synthesizer 12000A series
2) Techron 7550 Power Supply
3) Perkin Elmer 7280 DSP Lock-in Amplifier
4) Lakeshore Gaussmeter Model 450
5) Lakeshore Electromagnet Power Supply Model 647
6) Lakeshore Electromagnet
7) Ditom Microwave Circulator Model D3C 4080
8) Hewlett Packard Detector Model 8473 - Operating Frequency = 0.01-26.5GHz

Appendix D - Diagram of Front Panel of FMR Measurement Software

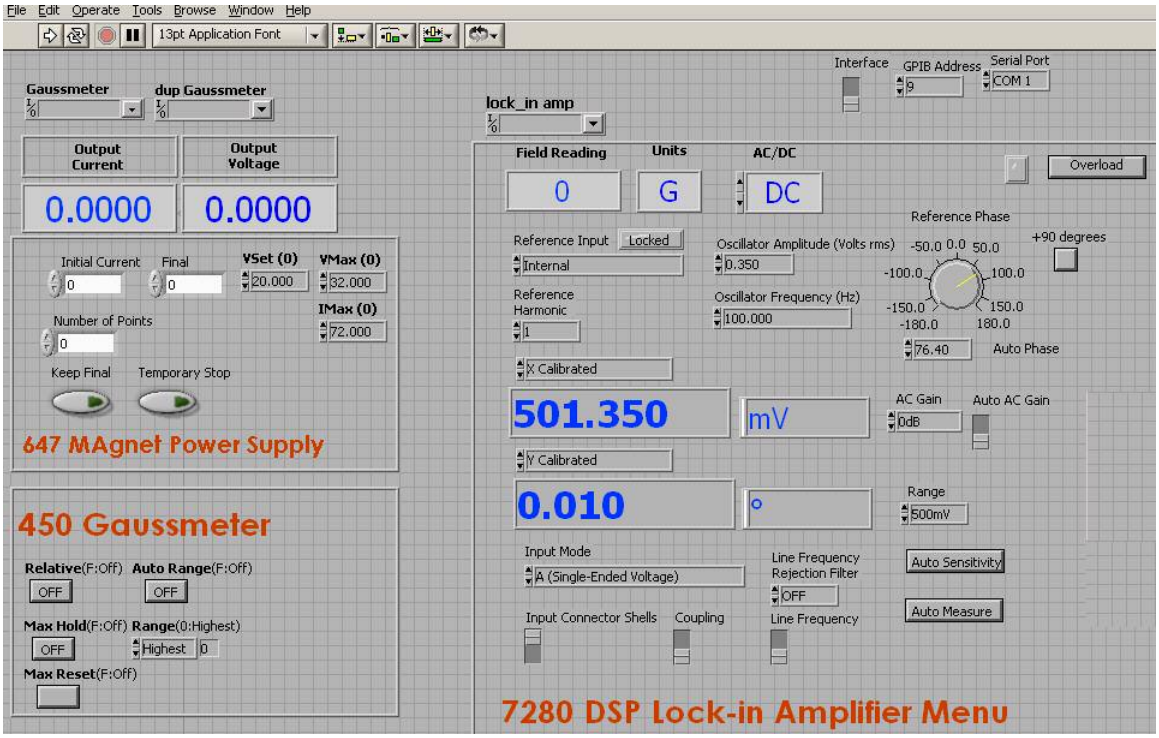

Appendix E - List of Parts of Imager System

1) Leica Power Supply for Tungsten Filament Light Source
2) E. Leitz, Inc. Short Arc Lamp Power Supply Model 1230
3) E. Leitz, Inc. Mercury Arc Lamp
4) E. Leitz, Inc. Polarized Light Microscope
5) QImaging Retiga CCD Camera
6) Numerik Jena LIE 5 Exposed Linear Encoders
7) National Instruments PCI – 6601 Counter Card

References

1. Tanaka, S-I “Longitudinal magneto-optic effect in Ni Films in visible and near infrared regions”. Journal of Faculty Engineering. University of Tokyo, series A, no. 6. 1968
2. Kahl, Soren. “Bismuth Iron Garnet Films for Magneto-Optical Photonic Crystals.” Doctoral Dissertation. Royal Institute of Technology. Stochholm, Sweden. 2004
3. T. Acihele et al. “Garnet layers prepared by liquid phase epitaxy for microwave and magneto-optical applications-a review.” Cryt. Res. Technol. 28, No7-8, 575-587. May, 2003.
4. V.J. Fratello, S. E. G. Slusky, C.D. Brandle and M.P. Norelli. “Effect o fDiamagnetic Subsitution on Growth-Induced Anistropy in (YBi)3Fe5O12.” J. Appl Phys. **60**. 718 (1986)
5. V. J. Fratello and Raymond Wolfe. Epitaxial Garnet Films for Nonreciprocal Magneto-optic Devices. Chapter 3. Handbook of Thin Film Devices. Vol 4. Academic Press. 2000
6. Eschenfleder. A. H. “Magnetic Bubble Technology.” Solid-State Sciences 14. Springer-Verlag. New York. 1981
7. Denysenkov. V. “Bismuth Iron Garnet Films for Ferromagnetic Resonance Spectrometer.” Doctoral Dissertation. Royal Institute of Technology. Stochholm, Sweden. 2003
8. “Principle of Magneto-Optical (MO) Measurements.” http://www2.polito.it/ricerca/superconductivity/MO/principles_of_measurements.html. Oct.11, 2004

9. L. E. Helseth et. al. “Faraday rotation and sensitivity of (100) bismuth-substitued ferrite garnet films.” Physical Review B. 66. Aug. 2002
10. R. M. Grechiskkin et al. “High Resolution Sensitive Magneto-Optic Ferrite-Garnet Films with Planar Anisotropy.” Magnetism and Magnetic Materials 157, 305 (1996).
11. E. L. Dukhovskaya and Yu. G. Saksonov. “Calculation of structural parameters in compounds of the garnet type.” Sov. Phys. Crystallogr. 22(5). Sept-Oct. 1977
12. Ferromagnetic Resonance. S. V. Vonsovskii. Pergamon Press. 1966
13. “Magnetic Anisotropy and Magnetostriction Garnets.” P. Hansen in Physics of Magnetic Garnets. Ed. By A. Paoletti. Pp. 56-1333 (North-Holland, Amsterdam. 1978)
14. “Fundamentals of Magneto-optical Imaging.” Superconductor Laboratory. University of Oslo. http://www.fys.uio.no/super/mo/#mo. Oct. 2004
15. Kittel, C. “Introduction to Solid State Physics”. Seventh Edition. Wiley and Sons Inc. 1996
16. C. Krafft, J. Zhang, K. Marr, J.B. Dotellis, and I. Mayergoyz. “Forensic Imaging of Magnetic Tapes Using Magnetic Garnet Indicator Films”. Nota Scinece Series in Mathematics, Physics and Chemistry-vol 142, 2003
17. Agilent Technologies, APPCAD Beta site, http://www.hp.woodshot.com/, APPCAD v3.0.2
18. I. Nistor, C. Krafft, I.D. Mayergoyz. “Magneto-optic studies of garnets subject to rotating magnetic fields.” To be published in Journal of Applied Physics.

19. “Oriented Particulate Magnetostrictive Composites.” http://aml.seas.ucla.edu/research/areas/magnetostrictive/oriented-particle/Particle%20Orientation.htm. Accessed Nov. 2004
20. A.A. Jalali, S. Kahl, V. Denysenkov and A. M. Grishin. “Critical angles effect: Vanishing of cubic mangetocrystalline anisotropy in ferromagnetic resonance spectra.” Physical Review B 66 Sept. 2002
21. A.A. Jalali-Roudsar, V. Denysenkov, and S. I. Khartsev. “Determination of magnetic anisotropy constants for magnetic garnet epitaxial films using ferromagnetic resonance.” To be published in Journal of Magnetism and Magnetic Materials
22. R. Rojas, C. Krafft, I. Nistor, D. Zhang, and I.D. Mayergoyz. Growth Effects (Rotation Rate) on the Characteristics of Bismuth Substituted Lutetium Iron Garnet. J. Appl. Phys. Vol. 42. 2004
23. D.E. Lacklison, g.B. Scott, H.L.Ralphs and J. L. Page. “Garnets with High Magnetoopitc Figures of Merit in the Visible Region.” IEEE Trans. Mag. MAG-9, 457 (1973)
24. V.J. Fratello, S. E. G. Slusky, C.D. Brandle and M.P. Norelli. “Growth-Induced Anisotropy in Bismuth-Rare Earth Iron Garnets.” J. Appl. Phys. **60,** 2488 (1986)
25. V. J. Fratello. S. J. Licht. C. D. Brandle. H. M. O’Bryan and F.A. Baiocchi. “Effect of Bismuth Doping on Thermal Expansion and Misfit Dislocations in Epitaxial Iron Garnets.” J. Cryst. Growth **142**. 93 (1994)